UNIMORE
UNIVERSITÀ DEGLI STUDI DI
MODENA E REGGIO EMILIA

UNIVERSITY OF MODENA AND REGGIO EMILIA

"Enzo Ferrari" Department of Engineering

Master's Degree in Adavanced Automotive Engineering

Analysis of CFD methodologies applied to a high-pressure H_2 injector in support to the design process

Supervisor:
Prof. Stefano Fontanesi
Co-supervisor:
Ing. Giuseppe Cicalese
Ing. Veronica Patrizi
Ing. Sara Vongher

Candidate:
Pierluigi Maria Teotini
Student ID 179211

ACADEMIC YEAR 2025/2026

Abstract

This thesis presents a computational fluid dynamics (CFD) investigation of a high-pressure hydrogen injector developed in STAR-CCM+, with the aim of evaluating the capabilities, limitations, and computational efficiency of different numerical methodologies for predicting injector performance throughout the operating cycle. Particular attention is devoted to assessing their suitability as design-support tools capable of providing both quantitative predictions and physical insight into the complex flow phenomena governing the injection process. Two modeling strategies were considered: a steady-state (SS) approach based on discrete needle-lift configurations, and a Dynamic Fluid Body Interaction (DFBI) model employing an overset mesh methodology to model the needle motion from the balance of fluid and external forces. The steady-state methodology was first validated against experimental mass-flow-rate measurements and compared with an equivalent transient morphing model driven by the experimentally measured needle displacement. The objective was to assess the ability of the stationary approach to reproduce the experimentally observed injector behavior and to evaluate the extent to which steady-state simulations can capture the dominant physical phenomena predicted by a time-dependent formulation of the same problem. A simplified two-dimensional DFBI simulation campaign was subsequently carried out to further investigate the capability of a force-driven modeling approach to reproduce the cause-and-effect mechanisms governing injector dynamics and performance. An overset-mesh strategy was adopted to handle the needle motion, overcoming the limitations of the morphing technique in configurations involving contact or near-contact between moving and stationary walls. Mesh-sensitivity analyses were also performed to assess the influence of overset-grid resolution on solution accuracy, numerical stability, and computational cost. The results were then compared with those obtained from the steady-state methodology, highlighting the potential of stationary simulations as efficient and reliable tools for preliminary design studies. In contrast, the transient approaches proved more suitable for investigating complex unsteady and compressible-flow phenomena, providing deeper physical insight and making them particularly valuable for detailed design verification and final optimization.

Contents

List of Figures

List of Tables

1. Introduction

The internal combustion (IC) engine, one of the most common thermal machine spread in the world throughout a wide range of application fields (cars, on- and off-road commercial transports as well as industrial and power generation applications), is facing and undergoing a rapid technology revolution due to the recent stringent emission legislations and deadlines implemented in several countries [1]. This rapid technological change is particularly affecting the transportation field, where the road vehicles sector is considered by the European Environmental Agency (EEA) one of the main responsible of the greenhouse gas (GHG) emissions [2]. As a matter of fact, the growing concerns about the environmental pollution led these increasing stringency regulations to push the research and development towards advanced and more complex solutions, which in some cases are very expensive and require to solve some practical issues. Indeed, even though many different strategies has been adopted to optimize the performances of the standard IC engines, the extremely low CO_2 emissions requirements are guiding the development towards several new technologies, including vehicle electrification or use of new innovative and zero-emissions fuels technologies (such as bio-fuels and e-fuels). In particular, the latter ones appear to be the most promising in guiding the gradual decarbonization process in the short-term period, with the hydrogen application to the well-consolidated engine technology getting more and more popularity.
In this complex and challenging scenario, the Computer-Aided Engineering (CAE), and in particular the Computational Fluid Dynamic (CFD) provide the required advanced approach to analyze the new different technologies and compare the several configurations to finally select the most promising solution, thus allowing to investigate the influence of the new technical solutions and guide the design process through the higher accessibility and feasibiity of the virtual environment.

1.1 Hydrogen engines and injectors

As anticipated, the current demanding constraints on the decarbonizations of the transport sector push research and development to find new alternative eco-friendly propulsion systems. In the recent year, as endorsed by legislations, electrification has been identified as the key technology

to achieve this ambitious goal [3]. However, the transition to fully electrified mobility is proving to be more challenging and time-consuming than expected, due to the lower autonomy of batteries compared to the one of the typical powertrains technology, as well as due to what concerns power and material supply and recycling of the battery components. For this reason, the development of zero-emissions propulsions systems based on existing well consolidated technology, such as the internal combustion engine (ICE), have gained a higher central role in this transition process. In particular, hydrogen-based propulsion systems [4] are promising to address the technological and market constraints. Hydrogen can not only be used as energy carrier to power Fuel cells Electric vehicles (FCEVs) without overloading the grid, but also can work as fuels for the internal combustion engine ($H_2 - ICE$) in Hybrid Electric Vehicles (HEVs) exploiting the well-consolidated engine technology whose established know-how and production lines would reduce the complexity and maintanance cost of the new powertrain, accelerating at the same time the the decabornization process demanded. Hydrogen as fuels has several advantages over gasoline, apart from zeroing carbon oxides emissions: for instance, the larger flammibility range along with the higher laminar flame speed allow the engine to operate with lean air-fuel ratios (λ) with benefits on engine efficiency but increasing the risk of knocking or backfiring due to the lower ignition energy.

One of the most critical aspects regarding the desing of ($H_2 - ICE$) consist in the choice of the ignition strategy. According to the arrangement of the fuel injector, ICE can be classified in two main families: port fuel injection (PFI) architectures and direct injection architecture (DI). In the former, the hydrogen injection take part inside the intake port of the engine, while in the latter the fuel is directly injected inside the cylinder after the intake valve closing. In the case of hydrogen, the DI architecture has been demonstrated the most promising solution, because of its property in solving the main drawbacks of the PFI architecture, such as the lower volumetric efficiency and backfiring problems [5]. As a consequence, the injector play a key role in the conversion of the old engine technology into a hydrogen based one. Indeed, because of the lower density of the hydrogen, the injectors must be able to deliver large volumes of gas in very short period to guarantee the necessary amount of mass in the cylinder. This can be achieved by acting on the design of opening head of the injector needle. This component usually present either an inward-opening shape or an outward-opening one. The latter, providing larger cross sections for the flow, allows to achieve more consistently the mass flow requirement. Moreover, a mixture stratification is expected in the

DI architecture that strongly depends not only on the injector arrangement but also in the timing of the injection. As a consequence, the injector and the optimization of the injection system point out how this component represent one of the key factor and challenges of the design of ($H_2 - ICE$) to ensure the correct efficiency of the machine.

1.2 Role of numerical simulation

The complexity of the innovation of the well-esablished ICE requires proper combination of different development tools to manage and investigate the numerous factors and concept ideas within a limited financial and temporal framework. In this scenario, the integration of numerical simulations in support to experimental campaigns becomes relevant. The role of the virtual design in the desing proces, indeed, has increased more and more thanks to the improvement of the computational power and the further development of simulation softwares, that allows to investigate and explore different design choices in very short-times, without the need of expensive and time-consuming experimental campaigns [6]. As a matter of fact, in front of the complexity of the modern engine development, the use of the CAE, especially the computational fluid dynamic (CFD) has become an unvaluable tool in supporting and guiding the design process. The CFD, the branch of the fluid mechanics that deals with the numerical solution of the partial differential equations that govern the heat transfer and the fluid flow, allows to study and reproduce the fluid behavior in order to evaluate its effects on the application under investigations. To achieve this goal, the governing equations of fluids are solved in a discretized fluid domain to reduce the original partial differential equations into an equivalent algebraic form to be numerically solved, by means of suitable optimized algorithms, via computers. In this way, it is possible to take advantage of the computational power of the calculators to obtain reliable approximated solutions of the flow behavior and dynamic of very complex systems without extensive and time-consuming campaigns on test benches. This explain why integration of such numerical tool in the design process of thermodynamic systems like the $H_2 - ICE$ is so crucial: numerical simulations not only allow a larger comprehensive insight of the system under investigation, delivering information impossible to obtain via measurements, but also turn into a valuable instrument able to guide both the early-design phase as well as the optimization of the settled geometries, by providing a deep insight of the processes occurring within the engine and

related components, other than analysing the effect of geometrical and control factors [7]. Indeed, the analysis of all the small different variable play a key role for a successful development, resulting instead unfeasible on a classical experimental campaign. Hence, the possibility to virtually test many different solutions allows to increase and support the design decision process during the development of the product. The CFD accomplishes then a dual role in the development process: as a simulation device (to provide insights of the transient phenomena occurring inside the system) and as a measurement tool (extension of the experimental tests). Its success can be summed up in the benefits that this numerical tool leads to the design process in terms of:

- **Cost-effectiveness:** Providing an exensive matrix of virtually tested configuraions results to be extremely less expensive than building and testing multiple physical prototypes;
- **Speed:** Results can be obtained in hours, providing rapid insights of many different configurations;
- **Detailed analysis:** Allows to obtain specific quantative data and enables in depth analysis of complex phenomena that are difficult to measure experimentally;
- **Problem-solving:** Helps identify and fix design flaws even in late stages of development.

Nevertheless, the computational effort and time of such numerical tools is usually extensive and scale with the complexity and the level of details required. For this reason, in the whole design process, the typical demanding 3D-CFD simulations are coupled with more light 0D-1D simulations of the engine system and components to provide input/outputs or boundary conditions necessary to the other [6, 8]. However, when dealing with such numerical tools it is important to do not fall in the common "GIGO (Garbage In Garbage Out) error". The numerical simulations in fact can provide accurate results but sometimes even misleading informations if the model is not suitably tuned. That's why the correlation between numerical models and the experimental results is an aspect of overwhelming importance to assess the reliability of the outcomes of the simulation. Indeed, independently of the data available, the CFD model must accurately represent the test conditions, both from the geometry and the boundary condition point of view, and match the experimental data obtained in the test, as faithfully as possible. This correlation process, in general, consists in an iterative scheme of runs and result analysis (similar to that depicted in Fig. 1.1) finalized

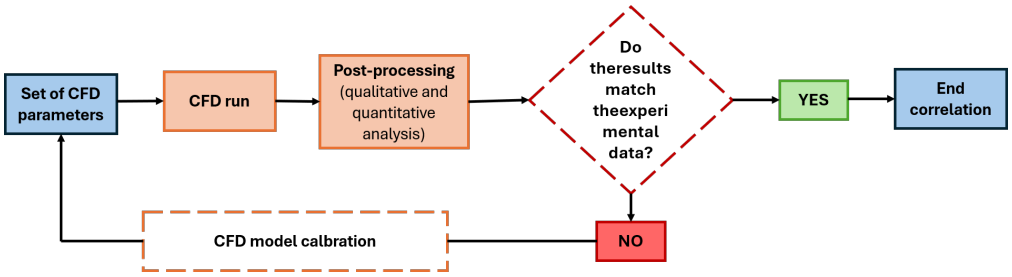

Figure 1.1: CFD model correlation loop

to the optimal setting of the CFD model, essential to build a robust virtual environment able to compete with the testing activities. This results usually in a time-consuming activity that scale with the complexity of the problem and of the modelling approach. However, in this way it is possible to check the reliability of the model used to reproduce the actual system working conditions, as well as assess the validity of assumptions made to achieve this goal (such as geometric or physical approximations) with the purpose of reducing the computational cost of the simulation.

1.2.1 Research activity goal and approach

Starting from this overview, the goal of the thesis activity is to study and compare different CFD methodologies available to predict the performances of a H_2 injector and return significant outputs for the design of a needle opening system, based on an electro-magnetic input. In particular, the main objective is to evaluate the reliability and cost-effectiveness of the various methodologies in providing accurate results in the different phases of the design process, with particular attention to the early ones. This is achieved by comparing the precision of the different models in matching the experimental data available, as well as by investigating the coherency of the related outputs of interest, which are intended to be used as inputs for most simple 1D-models built and set up to guide the design process. The main interested outcomes on which this research is focused on are represented by the mass flow rate, that the injector is able to deliver, and by the set of axial component of the forces acting on the different parts of the needle, with particular interest in the resultant of the pressure distribution. The interest in quantifying the force magnitudes, especially the fluid ones, is mainly driven by the need to tune properly the exciting force of the needle opening system.

On this purpose, two main approaches were considered:

- a **displacement based steady state approach**, where the flow conditions at regime for discrete working configurations of the needle (geometrical and physical) are analyzed and compared with an equivalent unsteady model, accounting for the not detected transient effects, to evaluate the margin of accuracy gained with respect an increased level of complexity;

- a **force based unsteady approach**, to account instead of the dynamic and transient effects provided by the external actions causing and affecting the relative motion between parts,in order to evaluate the reliability of the virtual development in predicting the cause-effect relationship chains

The second approach,in particular, classifies in two main strategies according to the technique used to take into account and reproduce the parts motion:

- **Morphing technique:** parts relative movement is accounted by moving the mesh vertices in response to the displacement of the boundaries;

- **Overset technique:** part based method where the independent mesh of each moving component is rigidly moved according to the displacement computed without changing the mesh vertices original position;

For this kind of activity only the overset technique is deeply investigated for its higher potentialities, while the morphing strategy is used, similarly to the the first approach, as numerical comparison. These analyses are supported by several experimental traces. To accurately reproduce the working condition of the injector along its cycle, the pressure profile of the inlet pressure was provided as input for the simulations. Secondly, the trajectory of the injector valve was measured to provide the lift profile for the displacement-based methods with the purpose of extrapolating the discrete working conditions for the steady state simulations and driving the respective transient simulations. However, due its natural property of being the effect of external actions, this data was used also as reference profile to compare the lift obtained by the unsteady force-based simulations. A trace for the experimental mass flow rate (MFR) was instead provided not only to evaluate the accuracy of the models in determining one of the target parameter but also to check their reliability of the model in providing the results under investigation, according to the "GIGO" principle. Finally, a parametrized profile of the exciting magnetic force of the needle was given to determine the

driving force of the force-based simulations. Each of these traces, coupled with the proper level of complexity of the model, enable to verify different cause-effect relationship, fundamental to check the reliability of the results. The MFR variation, for instance, depends on the value of the feeding pressure and of the cross sections (which in turn are strictly related to the needle displacement - "lift"), whereas the external actions are responsible of the valve motion that in turn is going to affect the flow rate of the injector. Thus explaining the importance of reference role, beside of input, of these experimental traces.

The whole analysis of the different CFD approaches used to reproduce the behaviour of the H2 injector has been carried out entirely via the Siemens DISW's commercial software of 3D-CFD, STAR-CCM+. Therefore, for what regard in particular the study of the unsteady approaches, the numerical investigation will take advantage of the consolidated techniques that the software provides to reproduce the dynamic of the component in motion and the resulting transient phenomena.

2. Basics of CFD

The Computational Fluid Dynamic deals with the numerical solution of the governing equations of fluids (Navier-Stokes equations), a set of non-linear partial differential equations for which a closed analytical solution does not exist yet, except for very specific and simple cases. However, the analysis of the fluid behavior and and its interactions with the surrounding bodies is become extremely important for the engineering development, especially from an optimization point of view. Consequently, even a not exact but approximated solution of this set of equations is considered useful, provided that the discretization errors and the modeling assumptions introduced for the numerical solution are bounded and reliable. Indeed, in order to numerically solve the Navier-Stokes equations via the power of calculators, the original governing equations must be turn into an equivalent algebraic form by approximating the complex mathematical operators (such as derivatives and integrals) such that they might be numerically handled. Moreover, the complex multiscale nature of turbulence requires to introduce some simplifying assumptions in order to model all the different scales of motion and reduce the computational cost that otherwise would be demanded by the direct resolution of all the degrees of freedom prescribed by the N-S equations. The success of CFD in providing approximated but reliable and accurate solutions, especially in terms of engineering applications, integrated this computer aided engineering (CAE) tool in the design process both in early and late stages of developments as already anticipated in 1.2 Nowadays, this numerical instrument is such structured that all the modern commercial software, like STAR-CCM+, includes all the different phases of a typical CFD workflow in one single environment to speed up and smooth the process. The different operations required to perform a complete CFD analysis can be classified in 3 steps:

1. **Pre-processing:** preliminary phase dedicated to the definition of the fluid domain geometry to analyses, the consequent discretizaion into a "mesh" and set-up of the physical properties, boundary conditions and solver features;

2. **Processing:** it is the actual resolution of the numerical N-S equation on the generated fluid domain performed by the calculator following specific algorithms developed on purpose; it is

automatically performed in background while the user check and wait for the convergence of the solution;

3. **Post-processing:** phase dedicated to the analysis and visualization of the results (field variabales such as velocity, pressure, etc..) aimed at extracting information and parameters useful to the design process

The following sections provide a concise introduction to the numerical solution of the Navier–Stokes equations, with particular focus on the solution algorithms and modeling techniques implemented in the subsequent analyses, necessary to understand the methodologies adopted in this work.

2.1 Numerical discretization

The behavior of fluid flows is governed by the fundamental principles of conservation of mass, momentum, and energy. These principles can be mathematically expressed through the Navier–Stokes equations, which constitute the foundation of the Computational Fluid Dynamics. The Navier–Stokes equations, represented by the system (2.1.1), describe the motion of viscous Newtonian fluids where, the momentum and the continuity laws together with the energy equation, form a coupled system of nonlinear partial differential equations

$$\begin{cases} \dfrac{\partial \rho}{\partial t} + \dfrac{\partial (\rho u_i)}{\partial x_i} = 0 \\ \\ \dfrac{\partial (\rho u_i)}{\partial t} + \dfrac{\partial (\rho u_i u_j)}{\partial x_j} = -\dfrac{\partial p}{\partial x_i} + \dfrac{\partial}{\partial x_j}\left[\mu\left(\dfrac{\partial u_i}{\partial x_j} + \dfrac{\partial u_j}{\partial x_i}\right) - \dfrac{2}{3}\mu \dfrac{\partial u_m}{\partial x_m}\delta_{ij}\right] + \rho f_i \\ \\ \dfrac{\partial (\rho e)}{\partial t} + \dfrac{\partial (\rho e u_j)}{\partial x_j} = S_E + \dfrac{\partial}{\partial x_j}\left(k \dfrac{\partial T}{\partial x_j}\right) - \dfrac{\partial (p u_j)}{\partial x_j} + \dfrac{\partial \tau_{ij} u_i}{\partial x_j} \end{cases} \tag{2.1.1}$$

where ρ is the fluid density, u_i is the i-th component of the velocity vector, p is the pressure, e is the total energy per unit mass, k is the thermal conductivity, f_i represents the i-th component of the body forces and S_E identifies the source terms of total energy. The nonlinear nature of these equations, together with the coupling between flow variables (pressure∼velocity), makes their direct analytical solution possible only for highly simplified cases. In practical engineering problems,

numerical techniques are therefore used to discretize the governing equations and transform them into a system of algebraic equations that can be solved computationally.

The numerical solution process begins with the discretization of the fluid domain into a finite number of control volumes, elements, or grid points, collectively referred to as *mesh*. The governing equations are then approximated over each discrete region using a suitable numerical method. Considering for simplicity a structured three-dimensional Cartesian mesh, to reach this goal, the flow variables are first "sampled" over the discrete spatial grid:

$$u(x, y, z, t) \Rightarrow \widetilde{u}_{l,m,n}(t) = \widetilde{u}(\widetilde{x}_l, \widetilde{y}_m, \widetilde{z}_n, t) \tag{2.1.2}$$

in order to start moving from a continuous to a discrete description of the problem, where $\widetilde{\mathbf{u}} = \widetilde{u}_{l,m,n}$ represents the approximated vector flow variable computed over the discretized fluid domain, with $(\widetilde{x}_l, \widetilde{y}_m, \widetilde{z}_n)$ representing the respective cartesian coordinates in the discretized grid. Then, by means of a suitable equivalent algebraic form of the differential operators the original set of partial differential equations (PDE) is reduced to a simpler system of ordinary differenial equation (ODE) to be integrated in time:

$$\frac{d\widetilde{\mathbf{u}}}{dt} = L(\widetilde{\mathbf{u}}) + N(\widetilde{\mathbf{u}}) \tag{2.1.3}$$

with $L(\widetilde{\mathbf{u}})$ and $N(\widetilde{\mathbf{u}})$ the spatial operators of the linear and non linear terms of the system of equation, respectively. By further introducing an appropriate discretization in time ($t \rightarrow t_n$) and a suitable numerical approximation for the general time integration step:

$$\frac{du}{dt} = f(u, t) \;\rightarrow\; u^{n+1} = u^n + \int_{t_n}^{t_{n+1}} f(u, t) \tag{2.1.4}$$

it is possible to finally obtain a complete set of algebraic equations of the form:

$$\underline{\underline{A}}\widetilde{\mathbf{u}} = \mathbf{b} \tag{2.1.5}$$

to be numerically solved by means of appropriate algorithms.

The most widely adopted approaches in CFD are the Finite Difference Method (FDM) and the Finite Volume Method (FVM). The FDM is the numerical technique that locally solve the partial differential equation of fluids by approximating the differential spatial operators with a suitable

discretized difference quotient 2.1.6, to obtain an equivalent algebraic version of the operator and of the original governing equations, similarly to previously provided example.

$$\left(\frac{du}{dx}\right)_i \approx \frac{u(x+\Delta x)-u(x)}{\Delta x} = \frac{\widetilde{u}_{i+1}-\widetilde{u}_i}{\Delta x} \tag{2.1.6}$$

In the finite volume approach, instead, the governing equations are integrated over each control volume and the Gauss' divergence theorem is applied to the volume integrals of the divergence terms to convert them into surface integrals, to allow the fluxes crossing the boundaries of each control volume to be evaluated. Considering the generic transport equation at the basis of the conservation laws, this translates in obtaining an equation of kind:.

$$\underbrace{\frac{d}{dt}\int_V \rho\phi\, dV}_{\text{Transient Term}} + \underbrace{\int_A \rho\mathbf{v}\phi\cdot d\mathbf{A}}_{\text{Convective Flux}} = \underbrace{\int_A \Gamma\nabla\phi\, d\mathbf{A}}_{\text{Diffusive Flux}} + \underbrace{\int_V S_\phi\, dV}_{\text{Source Term}} \tag{2.1.7}$$

where ϕ is the generic transported quantity, A is the surface area of the control volume, while Γ and S_ϕ are respectively the diffusive coefficient and the source term per unit volume of the transport. Setting appropriate value for these parameters the different conservation laws can be retrieved. By introducing a suitable algebraic form of the surface and volume integrals, expressing them as a function of the flow variables evaluated at the cell center (*mid-point rule approximation*), the equivalent algebraic form of the N-S equation is obtained. In particular, the volume integrals are approximated by the product of the mean value evaluated at the cell centroid (P) and the volume of the cell (V_i):

$$\int_{V_i} \mathbf{u}\, dV = \mathbf{u}_P\, V_i \tag{2.1.8}$$

whereas the surface integrals are approximated as a function of the mean value of the flux at the face center (J_k^ϕ)

$$\int_{\partial V} \mathbf{J}^\phi\, d\mathbf{A} = \sum_k \int_{A_k} \mathbf{J}^\phi\, d\mathbf{A} = \sum_k J_k^\phi A_k \tag{2.1.9}$$

whose value is actually extrapolated as interpolation of the known flow variable at the cell centroids. Among the aforementioned mesh-based discretization techniques, the FVM is particularly popular in industrial CFD applications because it ensures strict conservation of mass, momentum, and energy at the discrete level. Indeed, by making use of the divergence theorem, which reduces the volume integral contributions to the net fluxes at the surfaces of each control volume, the flux entering a given volume is identical to that leaving the adjiacent one through the same shared boundary,

making this method conservative by construction. Moreover, since the integral formulation of the N-S equation can be prescribed for control volumes of any shape and size, this approach proves more consistency than the FDM in discretizing geometries of any complexity, allowing such kind of framework to be formulated even for unstructured meshes.

2.2 Turbulence models

For turbulent flows, direct numerical resolution of all turbulent scales is generally computationally prohibitive for engineering applications. Consequently, a modelling approach to turbulence was introduced to account for the effects of unresolved turbulent fluctuations building an alternative set of equation to the N-S equations where turbulence is partially or completely modeled, providing a coarser representation of the solution but at the expense of a lower computational cost. Different types of turbulence models exist according to the resolution of the problem desired to achieved and the way closure problem of turbulence is solved. The most common approaches include:

- **Reynolds-Averaged Navier–Stokes (RANS):** The RANS modelling approach, basing on the Reynolds decomposition of the flow variables ($u_i = U_i + u_i'$) in an average temporal value (U_i) and a fluctuating instantaneous part (u_i'), find an equivalent system of equation, to be solved with respect the mean flow variables only, that differ from the original governing equation for the presence of an additional unknown term (Reynolds stress tensor) which model the effects of the turbulent fluctuations as additional source of stress/dissipation. This formulation allows to drastically reduce the degrees of freedom of the turbulent solution by reproducing the average flow field with reasonably good results and small computational resources. Different RANS models exists according to the way the unknown terms are modeled to close the alternative system.

- **Large Eddy Simulation (LES):** the LES modelling approach is rather based on space of scale flow field decomposition, obtained by a filtering operation able to divide the spectrum of fluctuations in a large scales to be resolved and smaller (subgrid) scales to be modelled. The filter length Δ define the range of scales to be resolved. The result is an alternative set of equations to be solved with respect the large fluctuations only. Compared to the RANS

model, this model provide a more accurate representation of the flow field and of the turbulent flow due to the larger amount of information carried out by the large scale of motions, but at the expense of a larger computational cost.

- **Dethaced Eddy Simulation (DES):** the DES formulation of the N-S equations consist in a mixed LES/RANS approach that aims at taking the most of the two modelling approach in a single formalism. In particular the low computational cost of the RANS formulation is used to solve the near-wall flow conditions, whereas the improved accuracy of the LES model is used to resolve the turbulent flow structures in the wake regions without adding excessive computational cost.

Following the goal of this thesis activity, based on the definition of macroscopic effects of the flow (mass and forces due to pressure mainly), the RANS modelling approach is considered sufficient for the numerical formulation of the problem. In particular, among the available RANS models, the ones based on the eddy viscosity assumption, such as the k-ϵ and k-ω formulations, are considered. These models, expressing the Reynold stresses ($< u_i' u_j' >$) in the phenomelogical form of viscous diffusion:

$$\langle u_i' u_j' \rangle - \frac{1}{3}\delta_{ij}\langle u_k' u_k' \rangle = -2\nu_T \langle S_{ij} \rangle \tag{2.2.1}$$

where $\nu_T = \nu_T$ is the "turbulent/eddy viscosity " and $S_{ij} = \left(\frac{\partial u_i}{\partial x_j} + \frac{\partial u_j}{\partial x_i} \right)$ the strain rate tensor, allows to model the effect of the turbulent fluctuations on the mean flow as an increased flow diffusivity able to dump all the turbulent scale of motions. Then, by taking advantage of two additional transport equations to provide an estimate of the eddy viscosity, a final closed set of equation to resolved with respect the mean flow variable is eventually obtained. These two models, despite basing both on a definition of ν_T as a function of 2 scalar field able to describe the full spectrum of fluctuations, differ for the way they model the second variable they solve for, their treatment of the near-wall region, and their range of applicability. In particular, the k-ϵ model relies on the turbulent kinetic energy k_T and dissipation rate ϵ transport equations to define the turbulent viscosity, leading to a turbulence formulation characterized by a ill-definition of the near-wall region which require specif wall treatments to correctly capture the near-wall behaviour. The k-ω model, instead, replace the ϵ with the specific dissipation rate ω transport equation, obtaining a formulation able to numerically solve the boundary layer region down to the wall without any treatment but at the expense of a

higher computational cost and sensitivity of the free-stream boundaries to the turbulent properties of the flow.

2.3 Navier-Stokes solvers

An additional challenge in the numerical solution of the Navier–Stokes equations arises from the coupling between pressure and velocity fields. In incompressible and low-Mach-number flows, pressure does not possess an independent transport equation, requiring dedicated pressure–velocity coupling algorithms. Common approaches include the SIMPLE (Semi-Implicit Method for Pressure-Linked Equations), SIMPLEC, and PISO (Pressure-Implicit with Splitting of Operators) algorithms. These methods iteratively enforce mass conservation while updating pressure and velocity fields within each time step until convergence is achieved. The solution procedure employed by these solvers is based on reformulating the N-S equations in terms of a momentum and a pressure equations, such that the computation of the velocity and pressure fields are decoupled and integrated in time in a segregated manner, from which the name "segregated solver" originates. In this iterative procedures the momentum equation is first solved using the pressure field of the previous iteration (*predictor step*, obtaining a resulting velocity field that conserves momentum but not necessarily mass. This velocity field is then used to construct the pressure equation whose solution is used to correct both the pressure and velocity fields (*corrector step*) so as to enforce mass conservation. This procedure is iteratively repeated until the pressure and velocity corrections are considered negligibly small. In case of compressible flows the density variations and its coupling with pressure become relevant. The segregated solvers family is able to handle also mildly compressible flows. Here, the pressure correction algorithm for compressible flows is obtained by a simple extension of that for incompressible flows [9]. The difference is only related to variations in density which are accounted for by defining a density correction field ρ' and relating it to the pressure-correction field through a pressure-density relation.

An alternative approach to the sequential algorithm for the N-S equation, is represented by the so-called "coupled solvers", where the conservation equations for continuity and momentum and pressure and velocity corrections are solved simultaneously as a vector of equations. The result is a faster convergence rates of the flow variable with respect the classical segregated approach, but

the memory requirements are significantly enhanced due to the need of allocating huge matrices representing the full system of equations.

2.4 Mesh models

The numerical solution of the Navier–Stokes equations inherently introduces discretization errors, as the continuous governing equations must be approximated through discrete representations in both space and time. The accuracy and stability of the numerical solution indeed strongly depend on the numerical schemes adopted for the discretization of the different terms of the governing equations, whose level of approximation directly influences the compatibility of modelling results with real data. However, while round-off errors arising from finite numerical precision will always interfere the solution, the truncation errors introduced by the numerical schemes adopted can be minimized by improving the discretization of the computational domain (meshing). The discretization of the computational domain can be achieved with the application of three main different mesh types depicted in Fig.2.1: hexahedral (HEX), tetrhedral (TETRA) and polyhedral (POLY). All types of mesh elements are characterized by different numerical diffusion which directly influence the quality of the solution and time of convergence. However, POLY cells have recently been introduced to combine the advantages of HEX and TETRA elements: the low numerical diffusion and contained elements number of HEX and the highly-automated generation of TETRA alongside their higher suitability to more complex geometries. Indeed, the individual POLY element neighbors with more cells in comparison to HEX and TETRA, which improves the calculation of gradients and allows better heat and mass transfer through numerous faces. In consequence, the application of POLY mesh reduces the influence of numerical diffusion in case of the flow not perpendicular to any

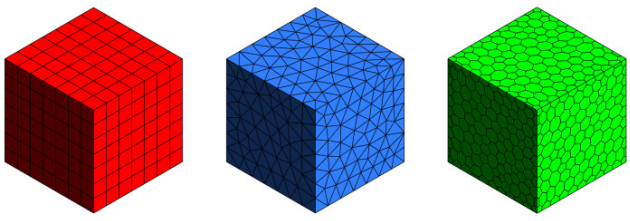

Figure 2.1: Examples of numerical mesh types: hexahedral (a), tetrahedral (b) and polyhedral(c) [10]

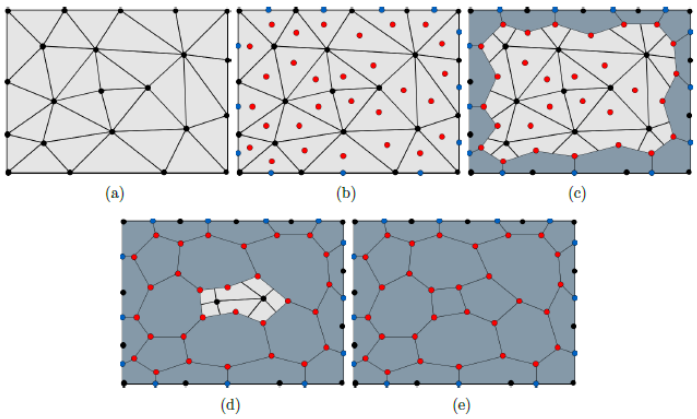

Figure 2.2: Polyhedral mesh process [12]

of the cell face. It is therefore advantageous in situations where no prevailing flow direction can be identified and leads to more accurate solution achieved with a lower cell count [10, 11]. The polyhedral mesher will be therefore used as reference for the mesh generation in this activity, for its general superior properties demonstrated. In Simcenter STAR-CCM+, the polyhedral core mesh is generated from an underlying tetrahedral mesh of the input surface, as shown in Fig. 2.2. A special algorithm mark the center of the tetrahedral cells (red dots in example), as well as the midpoints (blue dots in example) on the boundary edges (b), which are used to create the polyhedral cells on the surfaces starting from the boundary edges first (c) and from the outer layer then proceeding inward (d) until all polyhedral cells are created (e). Volume cells are then built from the surface mesh to the inner volume, with the *Volume growth rate* parameter determining how quickly the cell size increases with increasing distance from the surface.

2.5 Mesh motion

The numerical simulation of injection process requires the accurate representation of the relative motion between the needle and the stationary components of the valve assembly in order to detect the change in flow passages and the consequent flow field evolution produced by the needle displacement. In case of a transient simulation, the computational mesh representing the fluid domain must continuously adapt to the evolving geometry produced by the moving wall boundaries. This capability, commonly referred to as *mesh motion*, is a key requirement for transient CFD analyses

involving moving boundaries. The mesh motion is the numerical technique that allows to update the position of the computational domain while the solvers run. From a mathematical point of view, the Eulerian description of the conservation equations must consider additional fluxes in the convective terms that are introduced to account for change in shape and position of the boundaries, similarly to 2.5.1 where the transport term of a general ϕ quantity in presence of a moving boundary accounted by the grid velocity (v_g) is reported:

$$\int_{\partial V} \rho\phi(\mathbf{v} - \mathbf{v}_g) \cdot d\mathbf{S} \tag{2.5.1}$$

From the modelling point of view, instead, different mesh-motion strategies can be adopted depending on the nature of the displacement, the expected level of geometric deformation, and the computational cost that can be afforded. Simcenter STAR-CCM+ provides several motion models, which can either move the mesh rigidly, preserving the distance between any pair of vertices, or non-rigidly, allowing for deformation of the computational domain. These kind of motions can either be achieved by imposing the prescribed displacement to the boundaries or moving them in response to the displacement of a 6-DOF rigid body (DFBI model). Nevertheless, two main algorithms are used to perform the motion of the mesh and of its vertices:

- **morphing:** approach based on the continuous deformation of the computational mesh nodes to accommodate the prescribed motion of the boundaries that propagates into the surrounding domain, leaving the mesh topology unchanged while modifying the cell shapes and volumes in time.

- **overset mesh:** numerical technique that allows to simulate motion in a simplified way allowing each component to have its own optimized mesh, which overlaps with a background mesh and which rigidly moving over that while exchanging the flow information through a suitbale interpolation procedure;

In the present work, the overset mesh methodology was the only mesh-motion strategy investigated in depth. The morphing approach was instead employed exclusively as a benchmark within displacement-driven transient and DFBI simulations, providing a reference for assessing the numerical consistency of the steady-state methodology and for comparing the performance of the alternative DFBI–overset formulation. Nevertheless, a brief overview of the morphing methodology is provided for the sake of completeness.

2.5.1 Morphing

The morphing algorithm employed in STAR-CCM+ redistributes the mesh vertices in response to the displacement of the boundaries, allowing for non-rigid deformations of the mesh. It operates through a set of control points originating from the grid vertices of the moving boundary, that can be considered as a cloud of points overlaid onto the mesh domain. Each control point has an associated distance vector that specifies the displacement of the point within a single time-step, which can be either set directly or computed from an input grid velocity. These displacements are then used to construct an interpolation field that, propagating the boundary deformation from the moving boundaries into the fluid domain, will drive the displacement of all the mesh vertices. The morpher result most appropriate for cases with moving boundaries characterized by small displacements, where the shape of the boundaries maintain. The relatively small topological preparation and straightforward implementation of this model with respect the overset algorithm, make this methodology particularly suitable for displacement-driven simulations when the displacement is known a priori. However, since it deals only with displacing the grid vertices, without acting on cell volumes, faces or edges, the mesh quality progressively deteriorates as the deformation increases, potentially leading to highly skewed cells and numerical instabilities. For this reason the morpher is generally put beside the aid of a *remeshing model*, which, basing on mesh-quality criteria, improve and optimize the spatial grid compromised by the vertex motion whenever the quality parameters fall below a certain threshold, thus resulting however in a higher demand of computational effort. Furthermore, morphing techniques are generally unable to handle situations involving contacts or overlaps between moving and stationary bodies, which limits their applicability during the complete opening and closing phases of an injector. In these cases, a *gap closure* model is also introduced to simulate the opening and closing gap that forms between two boundaries in relative motion without explicitly modelling the contact but increasing the complexity and the effort of the simulation.

2.5.2 Overset

The overset is a part-based CFD technique implemented in STAR-CCM+ to simulate the large relative motion between bodies in a more simplified way than the other meshing strategies available. This kind of mesh treatment allows each component to have its own independent, optimized mesh

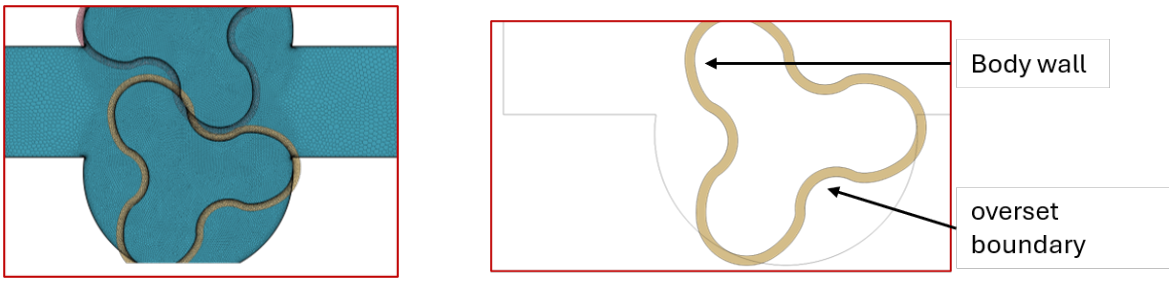

(a) (b)

Figure 2.3: Lobe Pump Tutorial []: (a) representation of overset meshes overlapping the background mesh; (b) overset mesh representation of the moving body

- termed *overset mesh* - which can overlap over each other in an arbitrary way within a common computational domain, referred to as *background mesh*. An example of this mesh classification is provided by the "lobe pump" tutorial of STAR-CCM+, represented in Fig. 2.3a, which allows to identify the main features of the overset model. Generally speaking, a typical overset simulation is in fact made up of two main kind of elements:

- **background region:** a region enclosing the entire solution domain (the blue region in the example);
- **overset regions:** separated independent regions surrounding each moving body that overlap the background mesh and rigidly move without deforming the original grid vertices (the yellow and purple tape parts in the example and in Fig. 2.3b);

Each moving body is therefore characterized by an external mesh enclosing the body walls and whose outer boundary (termed "*overset boundary*") defines the border of the overlapping zone across which the fluid properties are interpolated, allowing a data exchange with the background mesh eliminating the need to re-mesh the entire domain. This exchange of information between overset regions and the background mesh is performed by the "hole cutting process", an internal algorithm which couple these regions by marking as inactive all the background cells whose solution is obtained from the overset region. The result is a computational grid made up of all the active cells belonging to each different region, similarly to what shown in Fig. 2.4, and which update at each time-step according to the body motion. The overset is hence characterized by a higher level of independency of the meshes that enable a higher control and distribution of the grids quality and

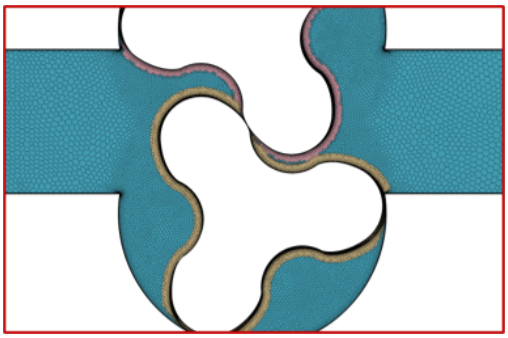

Figure 2.4: hole cutting operation: pseudo-subtract operation between background and overset mesh consisting in the deactivation of underlying background cells

resolution where actually necessary, usually around the moving bodies, without involving any mesh deformation during motion. Moreover, the single control of each part's mesh make this technique more suitable for case studies with walls in contacts involving a dynamic change in shape of the original boundaries, thanks to local activation and deactivation of cells. These characteristics make the overset approach particularly attractive for Dynamic Fluid Body Interaction (DFBI) simulations, where the body motion is computed as part of the solution rather than being prescribed. The increased flexibility, however, comes at the expense of a higher computational cost and a greater sensitivity to mesh-interface quality, requiring careful design of the overlap region and interpolation settings to ensure stable and accurate solutions.

3. Geometry

The numerical resolution of the discretized governing equations requires to define first the geometry of the fluid domain where the flow behaviour and body interactions will be studied. In case of specific devices, like the injector under consideration, this pre-processing operation involves the proper handling of the original geometry to obtain the desired volume of interest. This includes the removal of useless parts and faces, the creation of new functional bodies derived by the primitive surfaces and in some cases the cut-off or variation of the original geometric parts to accommodate the use of specific simplifying hypotheses for computational cost and complexity reduction purposes (bidimensionality or symmetry hypothesis for example). Moreover, some techniques, such as the overset approach, demand specific additional geometric features required by the model, according to how the algorithm at the basis builds and handles the parts and the related meshes, especially in terms of relative motion between boundaries.
The general considerations concerning the geometry preparation of the CFD models will be dealt in this chapter, leaving the treatise of the additional pre-processing operations specific for each methodology in their respective paragraphs.

3.1 Assembly overview

The injector considered operates under the action of a detached exciting pin, driven by an electromagnetic input, to open the valve and let the H_2 flow. It is therefore characterized by an inner actuator based on the action of a solenoid: in presence of an electric current, it generates an magnetic field that pushes the armature mounted on the exciting pin, which impacting on the valve needle, opens the injector. The actuation system results therefore separated by the flow ducts. Its action will be reproduced either by a predefined displacement either by the equivalent force, so the components of this assembly will be not useful to the numerical investigation and can be then neglected. The valve itself, instead, is a typical outward-opening valve (from now on referred to as "poppet") along whose needle is mounted a return spring, which close the injector in absence of a sufficient input, and a sealing rubber component, which divide the flow duct in two main chambers.

Figure 3.1: Initial injector geometry

This components will play a crucial role in the reproducing the motion, so particular attention is required in their modeling. This parts, moreover, are in direct contact with the flow, and represent the surfaces on which the fluid forces under investigation are acting on.

3.2 Geometry Preparation

The geometry preparation for the fluid-dynamic simulations began therefore with the complete STEP CAD assembly of the hydrogen injector, including all components positioned in their operational configuration, as shown in fig. 3.1. To extract the effective fluid domain required for the CFD analysis, all solid parts not directly involved in the flow path were removed, and the surfaces in mutual contact and wet by the fluid were merged into continuous surfaces to create new body groups. Additional upstream and downstream fluid volumes were appended at the inlet ducts and at the valve outlet to respectively impose uniform boundary conditions at the inlet boundary of the fluid domain and allow the flow to evolve freely downstream of the system. These geometric pre-processing operations, were focused on identifying two primary bodies, represented in fig. 3.2: the "injector casing", basically consisting of the external duct surfaces, and the "needle", shaped by the internal surfaces related to the moving valve. This latter, in particular, includes the seal body, modeled as rigid for the sake of simplicity, and the spring plate, which move together with needle. The first body, instead, represents the computational domain encompassing the whole fluid volume on which the software operates. This involves not only the outmost wet surfaces of the casings components, but also the internal faces of some moving parts, here modelled as rigid and fixed, that contribute to shape the fluid ducts of the injector, such as the faces of the bellow (an elastic component isolating the needle - exciting pin coupling) and of the spires of the return spring. The domain identified by these surfaces includes thereby the volume occupied by needle itself, the object on which the CFD

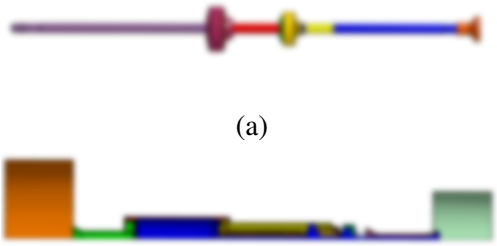

(a)

(b)

Figure 3.2: Needle part (a) and injector casing part (b)

analasys is dedicated to determine the forces. This parts distinction is important because it allows to point out the role of the internal moving bodies (the needle and a portion of the return spring) in the generation of the spatial grid where the governing equations are solved: in fact, the internal moving volumes represent the portions of the computational domain that must be subtracted from numerical solution. The resulting new inner boundaries will identify the needle walls on which the fluid forces are exerting their actions. The way in which this "subtract operation", or more precisely the way in which the needle boundaries are created and handled, in STAR-CCM+, is different for each methodology analysed, but all of them start from this two-parts configuration.

Last but not least, the intrinsic axisymmetry of the injector and its derived fluid domain was exploited to reduce the computational cost, modeling only the smallest representative sector of the geometry. Due to the presence of three circular arrays of holes with different angular pitches, the minimum repeatable segment corresponded to one quarter of the full geometry, preventing the use of smaller slices. Therefore, the axialsymmetric geometry was sliced such that to consider only one of the four resulting sectors. This operation divided the original spring spire in multiple independent arcs. From a modeling point of view, in order to do not aggravate the complexity of the motion provided by the flexible nature of this components, the spring body was assumed divided in two parts: a moving portion with the needle, represented by the first spire in contact with the spring plate, and a fixed portion belonging to the fluid domain part, embodied by the set of the remaining spires resulting from the slicing operation that were rectified for symmetry reasons. Despite of this deviation from the original geometry, the error introduced can be regarded negligible for the purpose of the present CFD simulations.

4. Steady State Simulations

The steady-state (SS) simulations deal with the numerical resolution of the governing equations and the related field variables without the usual the time-dependency relationship.

$$(p; v_i) = f(x, y, z, \not{t})$$

The resulting flow field obtained will provide a snapshot of the regime flow conditions provided by the set of boundary conditions selected. Disregarding the time-dependency means also to freeze the geometry in a particular configuration, getting rid of the relative motion between bodies. As a consequence, the SS simulations were conducted at several relevant valve-lift positions (Fig. 4.1) to evaluate the capability of the modeling approach to reproduce the experimentally measured mass-flow rate, for the respective prescribed pressure drop between the injector inlet and the valve outlet, other than investigate the reliability to foresee the entity of the fluid forces acting on the needle during the different phases of the injector stroke, irrespectively of the natural transient phenomena occurring during the opening and closing phases. Getting rid of the time-dependency, indeed, is a strong modeling assumptions that will turn into in a certain amount of error affecting the desired results. However, the goal of this methodology investigation is to quantify the magnitude of inaccuracy with respect the model complexity, in order to evaluate the reliability of the selected approach to provide correct design guidelines. In particular, in the first part of the activity, the results obtained, especially for the forces, will be compared with thsose of a separately developed transient model based on the morphing technique, thus providing a comparative numerical trace for the forces and the parameters for which an experimental correlation does not exist. These results

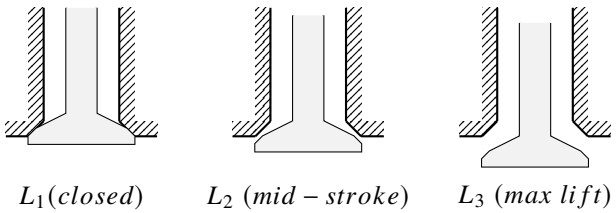

Figure 4.1: representative scheme of the different geometric configurations required by each SS simulation

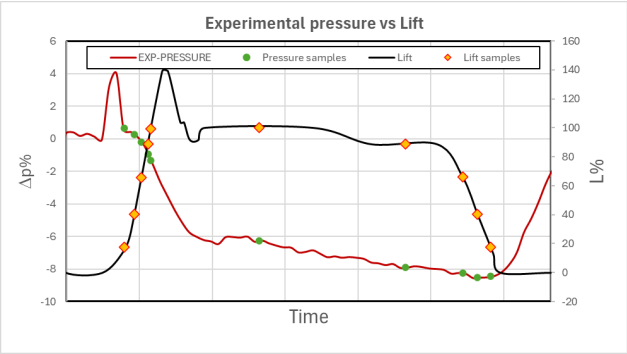

Figure 4.2: experimental inlet pressure plotted against the experimental needle displacement (L) in a cycle

are then compared at the end with the numerical technique analysed in the second part of the thesis work (the DFBI approach) to eventually provide a final overview of the performances and efficiency of the different models investigated.

4.1 Cycle configurations and conditions

As already said, he stationary nature of the SS model constrains the numerical investigation to the mere analysis of the regime flow conditions, namely the state of flow that would be obtained by keeping the injector in a fixed condition for an indefinite amount of time. Therefore, the present approach demands to identify specific geometric and physical conditions to be applied to once simulation at time to evaluate the predictability of the SS model to replicate the different states of the injector cycle without the time variable at stake. To achieve this goal, first of all, it is necessary to choose the relevant lift positions to analyse. They are selected from the experimental trace of the needle displacement, presented in Fig. 4.2. In order to reduce the number of simulations to run and increase the efficiency of the approach, the needle positions related to the opening and closing strokes were selected such that to coincide each other, a choice justified also by the intrinsic cyclic nature of the engine valve. In the present activity, only three lift positions were selected for the moving phases of the valve: an about 20%, 40% and 80% of the nominal stroke. The choice of these particular, almost equally spaced, values was essentially driven by the need of reducing the number of samples to compute, while providing at the same time a sufficient accurate representation of the needle dynamic, achieved through the linear interpolation of results arranged in their actual

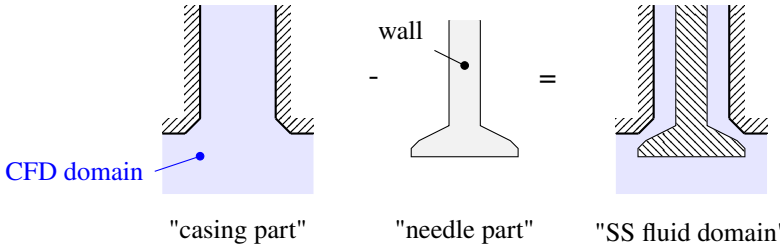

Figure 4.3: schematization of the Boolean operation between parts, aimed at retrieving the SS fluid domain for a specific displacement of the needle

position in time. The first stroke value, in particular, was selected as reference configuration for the starting and final needle conditions, being the former part of displacement interested by the seal decompression, impossible or more complicated to simulate. For what regard the valve holding positions instead, the single configuration corresponding to the maximum needle displacement is sufficient to characterize this phase. However, since a small retreat ($\sim$ -10%) was registered in the experimental campaign before the needle started to definitely close, this relative holding lift was tested as well, to be as accurate as possible in the results comparison, accounting it also in the set of opening configurations. From the geometric point of view, in order to obtain a single continuous fluid volume for each stroke position, the needle body was initially translated of the proper displacement prescribed by the stroke value downward the valve opening direction, and then a Boolean subtraction, schematized in fig.4.3, of the internal (needle) surfaces from the casing part volume was performed in the CAD environment to yield the final fluid domain for each of the prescribed SS analysis.

To fully characterize the operating conditions of each SS simulation, the boundary conditions associated with each geometric configuration selected were extracted from the experimental inlet pressure trace. Since the outlet pressure was kept constant throughout the analysis, the inlet pressure represents the only varying boundary condition among the simulations. Therefore, to reproduce the injector operating conditions as accurately as possible in the steady-state simulations and ensure consistency with the transient model, which follows the experimental profile in Fig.4.2, the inlet pressure corresponding to each needle-lift position was sampled from the experimental trace. As can be observed from the graphs, the pressure profile experience a rapid decrease from the nominal value once the needle opens, loosing almost a 10% of relative pressure. Dividing the operating

interval in 5 levels, it is possible to tabulate the boundary conditions for each lift position according to this simpler classification. The resulting table in Fig.4.4a shows that some configurations finds in an intermediate condition between adjacent levels of pressure. In these cases, the higher and the lower levels were considered respectively for the opening and the closing strokes. Thus doing it is possible to obtain the resuming table in Fig.4.4b that allows to optimize the simulation process. Indeed, dealing with a cycle where each geomtric configuration is characterized by at least two value of pressure it is possible to run a new simulation by simply varying one variable: either the Lift (for the same stroke) either the pressure (for equal position belonging to different strokes). For the holding lift positions, the same level of pressure, equal to the average experienced value, was considered for the sake of simplicity. The set of (L,p) pairs derived so far will be then used as reference for the definition of the geometric configurations and boundary conditions when setting the different SS simulations.

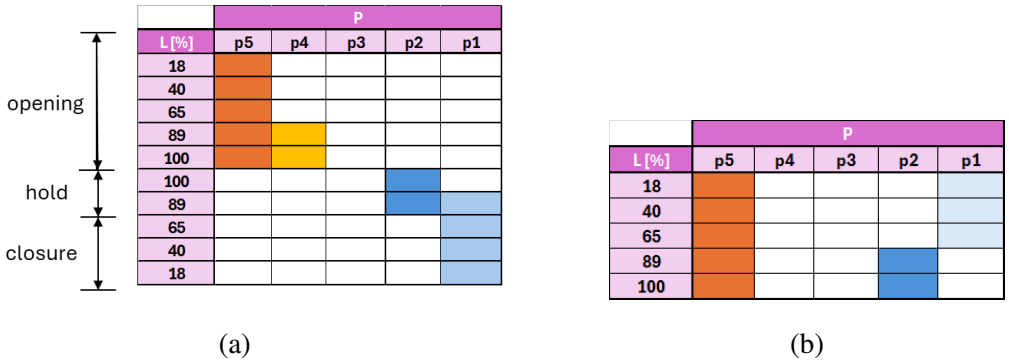

(a) (b)

Figure 4.4: sampled inlet pressure along the cycle for each stroke position of interest

4.2 Mesh

Once obtained the fluid domain from the subtract Boolean operation, the resulting geometry is converted in a CFD geometric counterpart to generate the associated "*Region*" on which the mesh is built. The mesh generation for these simulations was carried out according to the same strategy employed for the morphing comparative model. This choice comes from the desire to ensure as much numerical correlations as possible between models, in order to reduce the number of variables at stake and to retrieve the lonely effect of the modeling strategy. According to that, a *polyhedral*

Mesh Parameter	$L > 80\%$	$L < 80\%$
Base size	1 mm	0.6 mm
Targe Surface size	1 mm	0.6 mm
Min. Surface size	0.2 mm	0.12 mm
Max. Tet size	4 mm	2.4 mm
Surface Curvature	60 pts/circle	60 pts/circle
Surface Growth rate	1.05	1.05
Volume Growth rate	1.01	1.01
Prism Layer Near Wall Thickness	$5.0\ 10^{-5}$ mm	$5.0\ 10^{-5}$ mm
Prism Layer Total Thickness	0.2 mm	0.1 mm
Number of prism layers	20	10

Table 4.1: Mesh parameters for SS simulations according to needle's lift (L) value

mesher was chosen over the other mesh generator for its higher consolidated performance, already cited in Section 2.4, in providing good quality results with a limited amount of cells and shorter run times. The classic *Prism Layer Mesher* was selected instead for the discretization of the boundary layer (BL). In particular, the *"Wall thickness"* strategy was used to have more control on the construction of the near-wall region mesh, providing the first layer and total BL thickness. The mesh parameters, listed in table 4.1, follow the guidelines and results of a case study performed on a similar injector dealt in [13]. In particular, the mesh controls were initially selected to obtain optimal results for the largest lift configurations ($L > 80\%$), that are interested by a less critical supersonic condition in the narrowest sections. For smaller values of the strokes, instead, approximately 60% of the value of the different parameters was used to improve the solution convergence and reduce the flow oscillations through the finer grid obtained, especially at the seal and needle gaps. Indeed, the low lift configurations were characterized by a poor discretization of these flow sections, as the cell size was significantly larger than the local gap thickness.

To further address the insufficient mesh resolution, additional local refinement strategies were adopted. Surface controls were applied to the needle and seal surfaces to increase the mesh density in the regions where the narrow flow passages develop. Subsequently, volumetric refinements, like those shown in Fig. 4.5, were introduced around the needle-seat and sealing areas to support the

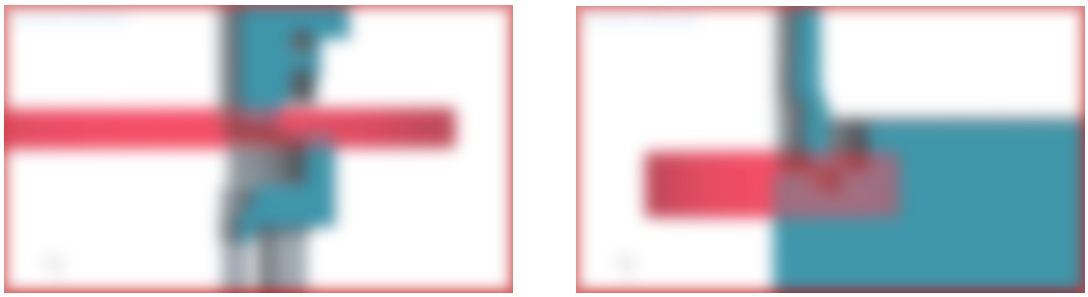

(a) (b)

Figure 4.5: Volume Refinement regions: (a) seal gap, (b) poppet

local surface refinements and further enhance the grid resolution within the critical flow passages. Figure 4.6 shows how the finer mesh configuration replaced the very few stretched cells, not suitable for the characterization of the the strong velocity gradients occurring in this regions. No dedicated refinements were applied instead along the jet direction, adequately resolved thanks to the small cell sizes resulting from the low volume growth rate. This choice was considered sufficient, as the focus of the analysis was not on the jet development itself, but rather on the pressure distribution along the needle walls. Finally, surface controls were applied to suppress boundary-layer meshing on the tank walls located upstream and downstream of the injector. Since these surfaces were not relevant to the objectives of the present analysis, this approach allowed the overall cell count to be reduced without affecting the accuracy of the results in the regions of interest.

Figure 4.6: Different grid resolution of the seal gap: on the left the coarser and streched cell distribution provided by high lifts mesh, on the right the higher mesh quality provided the finest mesh controls

4.3 Physic setting

Last step of the pre-processing operations, after the the preparation of the computational domain, concerns the set up of the physical properties of the model, including the definition of the fluid characteristics, of the boundary conditions and the solver settings. The physical models used to simulate the SS conditions of the hydrogen injector are listed below:

- **Time → Steady:** to get rid of time-dependency and obtain the stationary solution
- **Material → Gas:** to model the fluid (hydrogen) as a gas
- **Equation of State → Real Gas:** to account the deviation from the ideal gas equation due to high pressures, low temperatures and compressibility effects
- **Solver → Coupled Flow and Coupled Energy + Grid sequencing initialization:** higher capability to deal with large pressure difference and better convergence properties than segregated approach thanks to the potential flow initialization provided by the "*grid sequencing*" expert initialization solver option
- **Turbulence → RANS -** $k-\omega$ SST **model:** to solve NS equations and model the tubulent stress tensor with respect the mean flow variables only, modelling the full spectrum of fluctuations
- **Prism Layer treatment → All y+ wall treatment:** wall functions definition approach which adapt to local y+ value, suitable for intermediate low/high-Re situations

To reduce the computational cost associated with the solution of the governing equations, the fluid domain was modeled as single-component gas, coinciding with hydrogen. This simplification is justified by the steady-state assumption adopted in the present analysis. Although the injector operates under actual conditions with a mixture of air and hydrogen, it can be reasonably assumed that, once steady-state conditions are established, the air initially contained within the injector has been completely displaced by the hydrogen flow, resulting in a fluid domain entirely occupied by hydrogen. Under this assumption, species transport equations can be neglected, reducing the number of variables to be solved and improving computational efficiency and convergence behavior. Furthermore, a real-gas equation of state was employed instead of the ideal-gas formulation

Stagnation Inlet	
Total pressure	P_{in}
Total temperature	293.15 K
Turbulence intensity	0.05
Turbulent length scale	0.1 d_{ref}

Table 4.2: Inlet boundary condition (upstream tank)

to accurately capture the compressibility effects associated with the high-pressure operating conditions of the injector. Accordingly, the entire fluid domain was initialized with hydrogen. The thermophysical properties were defined using the *Thermodynamic Polynomial Data* available in the STAR-CCM+ material database for the evaluation of specific heat, while the dynamic viscosity was computed through *Sutherland's law* using coefficients available in the literature [14].

The choice of the solver was directly coupled to definition of the boundary condition for inlet and outlet boundaries. In CFD, the inlet section is usually characterized by boundary conditions able to correctly guarantee the correct mass flux into the numerical domain. This can be performed through different quantities, such as velocity, mass flow rate, or pressure, depending on the available experimental data and the desired representation of the physical system. Although the experimentally measured mass flow rate could have been used to define the inlet condition, it was intentionally retained as a validation parameter. Indeed, the mass flow rate represents a consequence of the pressure drop across the injector rather than an independent operating condition. For this reason, the steady-state simulations were configured to reproduce the experimentally measured pressure ratio across the injector, which, as discussed in Section 4.1, is determined solely by the inlet pressure, while the outlet pressure remains constant throughout the analysis. Accordingly, a *Stagnation Inlet* boundary condition was imposed at the upstream tank vent, while a *Pressure Outlet* boundary condition was applied at the downstream vent. The corresponding boundary-condition properties are summarized in Tables 4.2 and 4.3, respectively. The values of the turbulent parameters, in particular, follow the optimal set up defined in [13], whereas the pressure drop recorded by the experimental campaigns were directly applied through the constant values of p_{in} and p_{ou}, according to the tabulated values seen before in figure 4.4b, for each SS simulation.

Directly applying the operating pressure between inlet and outlet required to find a strategy

Pressure outlet	
Pressure	P_{out}
Total temperature	293.15 K
Turbulence intensity	0.05
Turbulent length scale	0.1 d_{ref}

Table 4.3: Outlet boundary condition (downstream tank)

to initialize the fluid domain without running into numerical divergence issues, thus affecting the choice of the solver. The main challenge associated with steady-state simulations is the absence of a physical transient evolution toward the final flow field. As a result, the solver must converge iteratively from an initial guess directly to the steady-state solution. While the final solution is theoretically independent of the initial conditions, an appropriate initialization becomes crucial in practice when dealing with highly compressible flows and large pressure gradients, such as those characterizing the present injector, to do not run into numerical instabilities problems. To address this issue, a preliminary multi-stage initialization strategy was investigated. The pressure difference across the injector was progressively imposed through a sequence of intermediate steady-state solutions, gradually increasing the pressure drop from an initially uniform pressure field in the fluid domain. This approach was tested using both segregated and coupled solvers, highlighting the strengths and limitations of each algorithm. The segregated solver exhibited faster convergence at each intermediate stage but was unable to robustly handle large pressure differences (only few hundreds of Pascals), whereas the coupled solver proved significantly more stable under high-pressure-drop conditions (ΔP of the order of few bars), although at a higher computational cost per iteration. Based on these observations, two alternative and more sophisticated initialization strategies were developed:

- a **transient-like approach** for the segregated solver, in which the boundary pressure was continuously varied as a function of the iteration number, which embodying the role of a temporal parameter, introduces a kind of time-dependency on the SS model;

$$p_{BC} = f(iter) \sim f(t)$$

- a **direct initialization** based on the coupled solver combined with a potential-flow solution.

The transient-like strategy, in particular, was carried out using an exponential dependency on the iteration number that lead the outlet pressure to the desired value, according to the following equation

$$p_{out} = p_0 - \Delta p \; e^{-\left(\frac{i}{\tau}\right)}$$

where "Δp" is the nominal pressure ration prescribed by inlet pressure of SS configuration considered, "i" is the current number of iteration, and τ is the "time constant" which define how rapidly the pressure decrease per iteration. This latter required values $\tau > 1500$ to guarantee the stability of the numerical solution. Although this approach successfully guided the solution toward the desired operating conditions, it required several thousand iterations and amount of time to reach convergence, due to the typical approaching behaviour of the exponential function. A superposition of faster exponential was then required to accelerate the process close the target pressure drop. Conversely, the coupled solver initialized through the potential-flow solution provided a more robust, automated, and computationally efficient procedure. For this reason, the latter approach was adopted for all steady-state simulations presented in this work.

Finally, to complete the definition of the boundary conditions, the symmetry properties of the original geometry were taken into account applying a *Symmetry* condition on the sliced lateral planes of the sector considered. All the other surfaces were defined as walls with a *No-slip* condition to properly account for friction effects, except for the outer tanks walls treated instead as *Slip* surfaces, since not relevant for the purposes of the analysis.

4.4 Results analysis

The results obtained for each (L,p_{in}) operating condition were mapped onto the injector cycle by associating each steady-state solution with the corresponding needle position measured during the experiment. The resulting dataset was then compared with both the experimental measurements and the predictions of the equivalent transient morphing model. This procedure provides a means of reconstructing a pseudo-transient evolution from discrete steady-state simulations, allowing a direct comparison between the two numerical approaches and the experimental data. Consequently,

the temporal information inherently missing from the steady-state simulations can be recovered, enabling an assessment of both the capability of the SS approach to reproduce the instantaneous flow field and its accuracy in predicting the overall evolution of the injector behavior throughout the cycle.

4.4.1 Mass Flow Rate comparison

Regarding the injector mass flow rate, the steady-state predictions exhibit a closer agreement with the experimental measurements than with the transient morphing results, as shown by the sampled green curve in Fig.4.7. In particular, the steady-state reconstruction reproduces the slopes of the measured mass flow rate trace with good accuracy during both the opening and closing phases of the injection event. Conversely, the transient model appears more sensitive to the needle-motion dynamics and to the displacement overshoots present in the experimental lift signal, which are not explicitly considered in the steady-state approach.

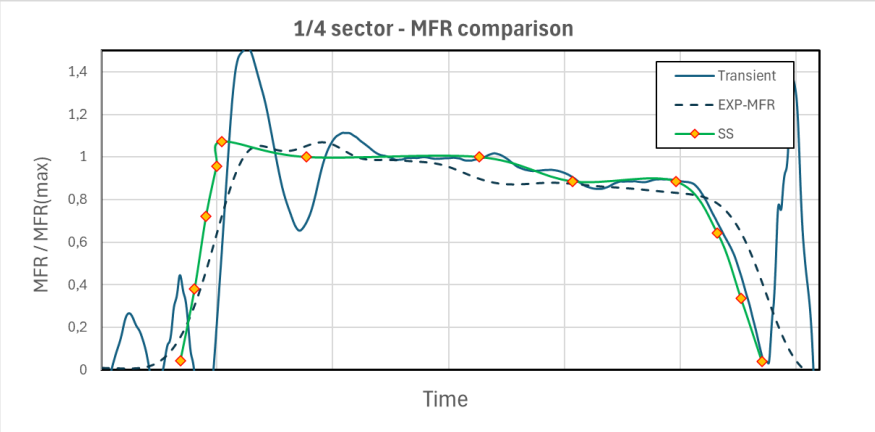

Figure 4.7: Normalized mass flow rate with respect to the maximum-lift (holding) experimental injection rate: comparison between the steady-state approach, the transient morphing model, and the experimental measurements.

This observation allows to assess the reliability of this approach in providing coherent results with the measurements of the experimental campaigns. Indeed, this behavior is consistent with the physics governing compressible flows under choked conditions. In such a regime, the mass flow rate is primarily controlled by the upstream pressure and the effective throat area according to:

$$\dot{m} = C_d\, A\, p_{up} \sqrt{\frac{\gamma}{R\,T}\left(\frac{2}{\gamma+1}\right)^{\frac{(\gamma+1)}{(\gamma-1)}}} \quad \rightarrow \quad \dot{m} \propto A * p_{up} \tag{4.4.1}$$

where C_d is the discharge coefficient, whereas γ, R, T denotes the thermodynamic properties of the hydrogen. Consequently, during the opening and closing phases, where the inlet pressure is assumed constant for each sampled operating condition, the mass flow rate varies mainly with the needle lift through the corresponding change in flow area. Conversely, between the fifth and sixth operating points, where the lift remains constant while the inlet pressure decreases, a reduction in mass flow rate is observed, consistently with Eq. 4.4.1. In contrast, the morphing approach is inherently more sensitive to the needle displacement, which acts as the driving input for the mesh motion, and to the flow-field evolution associated with the progressive opening of the seal. As a consequence, the transient solution exhibits pronounced fluctuations, partly inherited from the oscillations of the measured needle-lift signal and partly generated by the numerical computations and transient flow structures developing during the opening and closing phases of the injector. Regarding the holding phase, the steady-state results show excellent agreement with the predictions of the transient morphing model. This outcome is particularly significant, as it confirms the expectation that both modeling approaches should converge toward the same solution whenever the needle position remains nearly constant and the flow approaches quasi-steady operating conditions. Moreover, both of them accurately reproduce with a very small error the experimental trace in this range of positions, despite of the different timing. A similarly good agreement can also be observed during most of the closing stroke. As a consequence, these observations demonstrate that the predicted flow field is largely independent of the modeling strategy adopted, for these particular injector positions. This finding strongly supports the use of steady-state simulations for the analysis of injector performance. Indeed, the SS approach is capable of reproducing the relevant injector dynamic with accuracy comparable to that of the transient model, while requiring significantly lower computational resources and simulation time.

4.4.2 Fluid Force analysis

Having established the capability of the steady-state model to reproduce the experimental mass-flow-rate measurements and verified its consistency with the transient morphing approach, the analysis

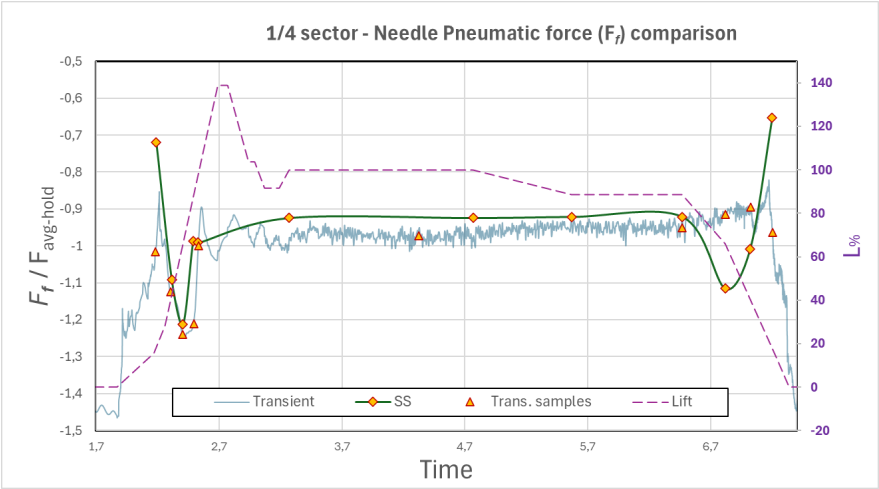

Figure 4.8: Models comparison of the normalized Fluid force with respect average demand prescribed by transient model at maximum operating conditions (holding positions)

can now focus on the primary objective of the CFD investigation: the fluid-dynamic forces acting on the injector needle. The resultant force exerted by the fluid on the needle arises predominantly from the pressure distribution over the various needle and valve surfaces perpendicular to the injector axis. The accurate prediction of these forces is of paramount importance, as they directly affect the design of the actuator system responsible for generating the electromagnetic force required to control the opening and closing of the injector. Therefore, comparing the force predictions obtained with the different numerical approaches provides valuable insight into their suitability for supporting the design and sizing of the actuation system. Since no experimental measurements of the fluid forces are available, the analysis cannot rely on a direct validation against test data. Consequently, the discussion will focus on the consistency of the predicted force trends and on the differences observed between the steady-state and transient methodologies, with the aim of assessing their capability to describe the fluid–structure interaction within the injector.

The steady-state samples of the total pressure force acting on the needle surfaces are compared with the predictions provided by the displacement-driven transient morphing model similarly to the mass-flow-rate analysis, as shown in Fig. 4.8. To facilitate the interpretation of the results throughout the injection cycle, the needle-lift profile has been superimposed in the background, providing a direct correlation between the force evolution and the needle position. At first glance, the steady-state and transient models show a remarkable level of agreement in capturing the overall

fluid-dynamic loading acting on the needle. Both approaches in fact predict a net closing force exerted by the flow, which is consistent with the expected behavior of an injector that has to be opened. A more detailed analysis of the three main phases of the injection cycle—opening, holding, and closing—reveals that the steady-state methodology remains highly reliable as long as the needle does not invert its motion, moving in opposite direction with the flow. During the holding phase, the two models exhibit an almost identical trend, predicting a nearly constant force level over time. Although the steady-state results systematically underestimate the force predicted by the transient simulation in this operating range, the discrepancy remains limited, with an average relative error of approximately 5%. Considering the simplifying assumptions underlying the steady-state approach, this level of agreement can be regarded as highly satisfactory. The consistency between the two methodologies is further confirmed by the flow-field comparison reported in Fig.4.10, where both models predict a similar jet structure and pressure distribution in the critical seal region. The opening phase is also reproduced with good accuracy by the steady-state reconstruction. Once again, the force level is slightly underestimated respect to the transient model, mainly due to the differences in the pressure-drop distribution among the internal chambers, highlighted in Fig.4.11, by the measurements of the numerical pressure probes distributed over fluid domain. Nevertheless, the resulting error remains relatively small over most of the opening range. Larger discrepancies are observed only at high needle lifts, where the flow undergoes a transition from choked to subsonic conditions. In this operating regime, the transient model captures the gradual evolution of the flow field, whereas the steady-state simulations converge directly to the fully developed solution. As a

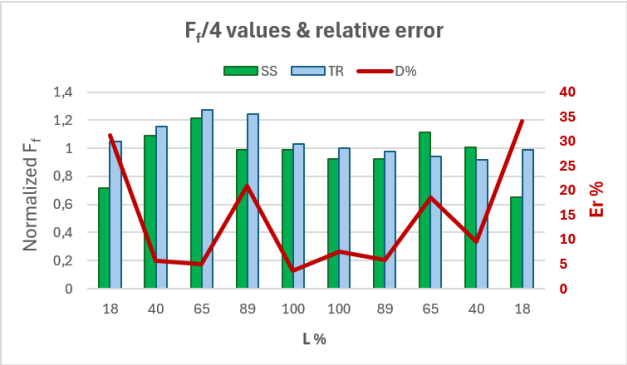

Figure 4.9: Fluid force values comparison between SS and morphing model with distribution of the relative error provided by the SS predictions

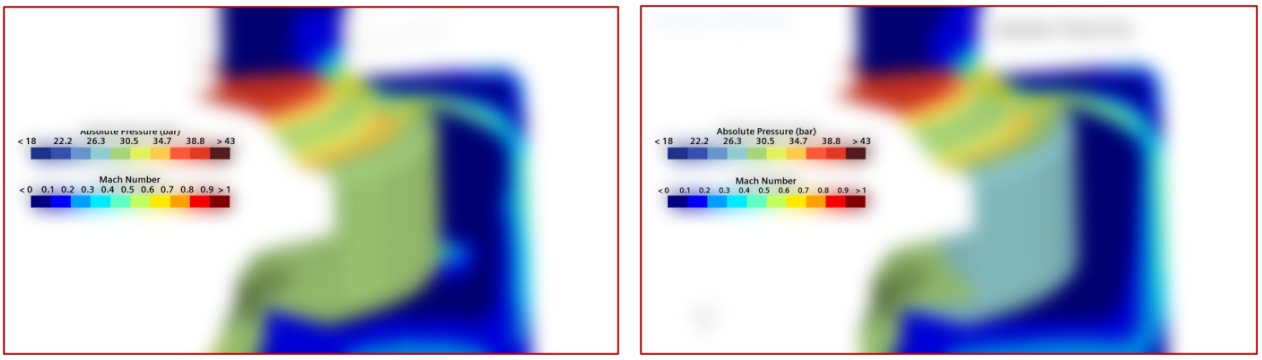

Figure 4.10: pressure distribution on seal surface and mach comparison at steady lifts, between morphing (left) and SS model (right)

consequence, the transient effects associated with this flow transition are less accurately represented by the steady-state approach, leading to an increased deviation between the two predictions, as can be observed from the relative error distribution in Fig. 4.9. The only significant discrepancy observed during the opening phase corresponds to the first sampled operating condition immediately following the opening of the seal. At this point, the force predicted by the steady-state model is significantly lower than that obtained from the transient simulation, despite this approach prescribes a decreasing trend toward the steady operating condition. The origin of this deviation can be identified examining again the pressure histories measured in the different injector chambers. In particular, the chamber located downstream of the rubber seal exhibits a markedly lower pressure level in the SS simulations. This discrepancy is primarily associated with the transient depressurization of the lower chamber, observed in figure 4.12, caused by leakage through the poppet valve during the seal-opening

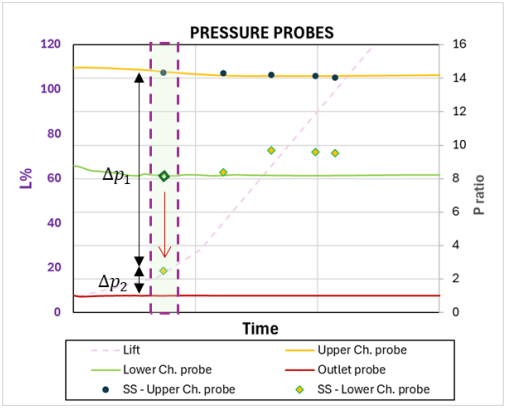

Figure 4.11: pressure probes models comparison - opening stroke

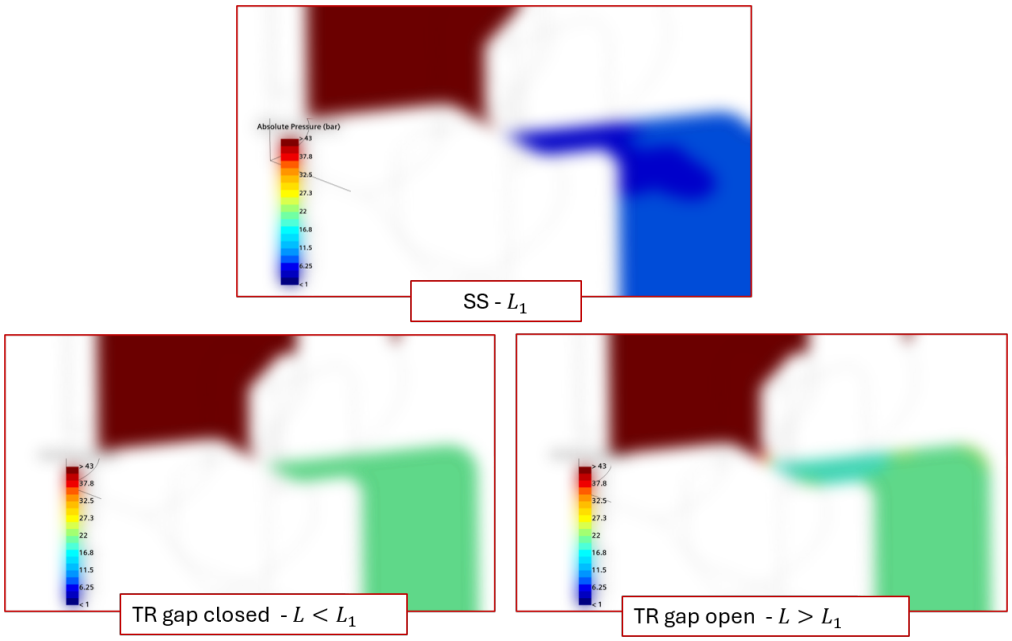

Figure 4.12: mid-chamber pressure field: during seal opening, transient model shows a depressurized mid-chamber from the previous cycle that slowly approach to the low pressure condition prescribe by the SS model

process, a phenomenon that cannot be captured by a time independent steady-state solution. As a consequence, the pressure distribution acting on the seal and poppet surfaces differs significantly between the two approaches. Since these components provide a non-negligible contribution to the overall force balance on the needle, the resulting fluid-dynamic force predicted by the steady-state model is less biased toward closure than that obtained from the transient simulation. This explains the large mismatch observed at the first opening sample, while preserving the overall consistency of the force trend throughout the remaining injection cycle. During the closing stroke, the interpolation of the steady-state samples predicts a trend that is almost symmetrical to that observed during the opening phase, with only a limited hysteresis resulting from the different kinematic conditions characterizing the two motions, namely the needle velocity, acceleration, and displacement history. However, the steady-state reconstruction progressively diverges from the transient prediction during the final portion of the cycle, when the needle retracts against an already established flow field. The largest differences, reaching approximately 15–20%, are observed at the onset of the needle retraction and near the complete injector closure. In the latter case, considerations analogous to those discussed for the initial opening stage can be invoked: the different pressure levels established

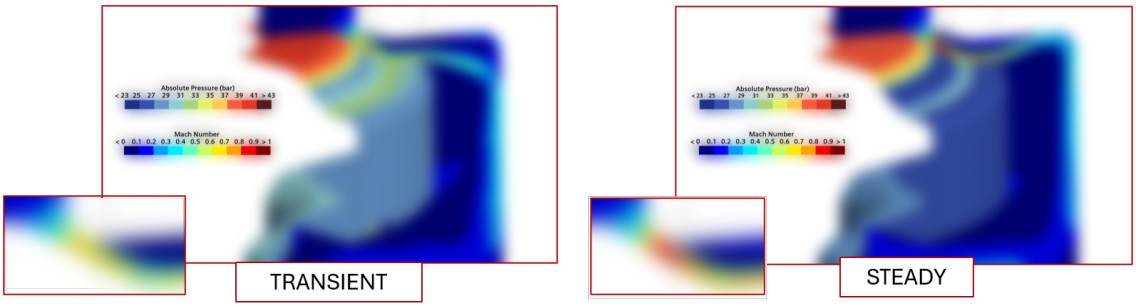

Figure 4.13: Example of the different flow topology and pressure distribution registered by the SS and transient methodology during the needle retraction phase

within the internal chambers lead to a different fluid force balance acting on the needle. For the intermediate lift positions, instead, the disagreement originates from the different treatment of transient effects by the two numerical approaches. Indeed, the transient model evolves from a previously stabilized flow field whose pressure and velocity distributions require a finite time to adapt to the needle motion. As a result, the flow retains a memory of the preceding operating condition while the needle is retracting. The steady-state simulations, on the other hand, directly converge to the fully developed solution associated with each lift position, neglecting any history effects. Consequently, not only the pressure distribution acting on the needle but also the structure of the emerging jet differ from those predicted by the transient model, as illustrated in Fig.4.13. The largest differences between the two numerical approached occurs therefore in the range of lifts where the needle motion is usually rapid, highlighting the limitations of the steady-state approach in reproducing flow conditions dominated by strong transient phenomena.

4.4.3 SS Conclusions

The results discussed so far allow several conclusions to be drawn regarding the applicability of the steady-state methodology and its competitiveness with respect to equivalent transient approaches. First, the excellent agreement achieved with the experimentally measured mass flow rate demonstrates the capability of the steady-state model to accurately reproduce this particular flow features governing injector performance. This level of accuracy, combined with the relatively simple setup and low computational cost of the simulations, makes the steady-state approach particularly attractive in guiding the design process. This conclusion is further reinforced by the comparison with the

morphing transient model, which provides a comparable level of accuracy in terms of mass-flow-rate prediction, but at the expense of substantially higher computational resources and a significantly more complex and time-consuming model-development procedure. While a steady-state analysis can be largely automated and executed through a series of independent simulations, the implementation of a transient morphing model often require extensive calibration and tuning efforts before reliable results can be obtained. On the other hand, the prediction of fluid-dynamic forces acting on the needle represents a more challenging task. The comparison with the displacement-driven transient model highlighted both the strengths and limitations of the steady-state methodology. Overall, a good level of agreement was observed between the two approaches, particularly during operating conditions in which the needle motion is either aligned with the flow direction or sufficiently slow for transient effects to remain limited. Under these circumstances, including the holding positions, the relative error generally remains below 5%, confirming the capability of the steady-state approach to provide reliable estimates of the fluid–structure interaction. Larger discrepancies were observed during phases characterized by strong accelerations, rapid changes in flow topology, or opposite relative motion between the needle and the already developed flow field. In these situations, transient phenomena and flow-history effects become increasingly important and cannot be captured by a sequence of independent steady-state solutions, leading to deviations that may reach 10–35%. Based on these observations, the steady-state methodology can be considered an effective and computationally efficient tool for supporting the preliminary design phase of hydrogen injectors. Its ability to provide accurate estimates of both mass flow rate and fluid-dynamic forces, together with its low computational cost, makes it particularly suitable for routine analyses and for generating input data for lower-order 1D/0D system models. Conversely, transient CFD approaches remain essential during the final stages of design optimization and validation, where the detailed investigation of highly unsteady phenomena, complex fluid–structure interactions, and compressible-flow effects is required. In this context, transient simulations provide a level of physical insight that is generally inaccessible through either steady-state analyses or experimental measurements alone.

5. DFBI - OVERSET 2D model

The Dynamic Fluid Body Interaction (DFBI) methodology represents a further level of physical fidelity with respect to the previously discussed approaches. Unlike the morphing technique, where the needle displacement is prescribed a priori and the mesh is deformed accordingly, the DFBI algorithm computes the body motion as part of the solution by coupling the fluid-dynamic forces and moments acting on a body with the external mechanical actions applied to it. The resulting motion is then transferred to the computational mesh through the overset-mesh approach, allowing the associated regions to move rigidly within the fluid domain without deforming the original grid. From a modeling perspective, this methodology moves one step upstream in the cause-and-effect chain governing the injector dynamic. Rather than prescribing the needle motion and observing the resulting flow field, the needle displacement emerges naturally from the balance between the electromagnetic force generated by the actuator, the mechanical forces exerted by the injector components, and the fluid-dynamic loads acting on the moving body. Consequently, the external actions, in particular the actuation one, become the primary inputs of the simulation, while the needle motion, mass flow rate, and fluid forces are obtained as outputs of the coupled fluid–structure interaction problem. The overset-mesh methodology was selected in place of the morphing approach to overcome the limitations associated with large mesh deformations and the progressive bodies contact between the moving and stationary components. By allowing the needle mesh to move independently of the background grid, the overset technique provides a more robust framework for handling the complex relative motion and surfaces interactions occurring inside the injector. The main objective of this analysis consists therefore in evaluating the capability of the DFBI approach to reproduce the experimentally observed needle dynamics and, consequently, the resulting mass flow rate and fluid-dynamic forces. Furthermore, the forces predicted by the DFBI model will be compared with those obtained from the corresponding DFBI morphing simulation in order to isolate the effects of the motion strategy itself and analyse the differences of the two methodologies when subjected to the same physical inputs. In particular, due to the increased computational complexity associated with mesh motion and the transient evolution of the flow field, the DFBI analysis limts to the study of simpler but equivalent two-dimensional model. This

simplified configuration significantly reduces the computational cost while preserving the main physical mechanisms governing the injector dynamics, thereby enabling an initial assessment of the DFBI methodology before extending the analysis to a more demanding three-dimensional model.

5.1 Bi-dimensional overset geometry

The geometry preparation required for the DFBI–overset approach differs from that adopted for the previous methodologies, while still building upon the same baseline two-parts injector model. Additional pre-processing operations were necessary to accommodate both the overset-mesh framework both the two-dimensional approximation adopted in this preliminary investigation. In particular, two main aspects had to be addressed:

- **overset mesh preparation**: the overset methodology relies on multiple overlapping meshes, derived by a suitably partitioned geometry into dedicated regions, where a a body-fitted grid surrounding the moving component is allowed to translate over a stationary background mesh
- **2D approximation:** the reduction of the original three-dimensional geometry to a two-dimensional domain requires appropriate modifications to the model orientation and topology in order to extract a representative planar section of the problem under investigation

As a result, the development of the overset model required a dedicated pre-processing study, largely based on the overset-mesh guidelines and tutorials provided by Siemens. Starting from the baseline sliced CAD model, the volume corresponding to the injector casing was used to define the background mesh region, which encloses the entire computational domain and is subsequently overlapped by the moving needle mesh. Regarding the overset region, which represents the independent mesh surrounding the moving body and that exchanges information with the background grid through the overlapping zone, the original needle geometry was replaced by a solid of revolution obtained by applying an offset to the outermost needle surfaces. This operation generates a shell-like body with a uniform thickness equal to the prescribed offset, which preserves the overall needle shape while removing fine geometrical details that are not essential for the definition of a simple and well-conditioned interpolation interface between the two meshes (a schematic representation of this procedure is shown in Fig.5.1). In this way, the original needle surfaces — required

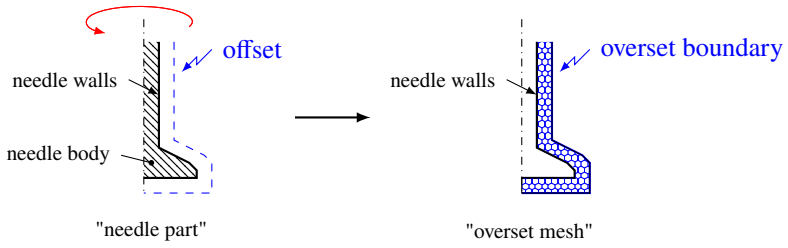

Figure 5.1: schematic representation of the overset region generation from the respective needle's part

for the evaluation of fluid-dynamic forces — are retained, while a surrounding overset envelope is introduced, whose external surface (the so-called "*overset boundary*") defines the interpolation interface with the background mesh. The offset thickness was selected to ensure that the overset region fully covers the gap zones throughout the entire needle stroke, thereby minimizing interpolation errors in these highly sensitive regions while still allowing a controlled and efficient mesh resolution. Moreover, it was determined in a way so that to maximize the cells dimensions of the minimum number of cell layers (≥ 4) required from the overset boundary in the interpolation area. Finally, the relative position of the two mesh components was initialized by placing the needle in its closed configuration, involving the seal compression, which was selected as the starting condition for the simulation. Once all geometric features required for the overset methodology have been prepared, a representative section of the three-dimensional model must be identified in order to extract an equivalent two-dimensional fluid domain for the reduced-order formulation. The main difficulty in this procedure arises from the presence of three distinct circumferential hole patterns, whose angular arrangement allows only partial, pairwise alignment within the eligible cutting plane. As a consequence, a fully consistent alignment of all the hole sets cannot be achieved in a single two-dimensional section, preventing the definition of the desired continuous and physically representative 2D fluid domain (see Fig. 5.2). On this purpose, the geometry of one of the misaligned hole patterns was modified in order to enforce coplanarity with the other two aligned sets, by projecting its features onto one of the symmetry planes of the quarter model. As shown in Fig. 5.3, this adjustment restores the missing flow passages within the selected cutting plane, thereby enabling the definition of a continuous two-dimensional section that is representative of the original three-dimensional fluid domain.

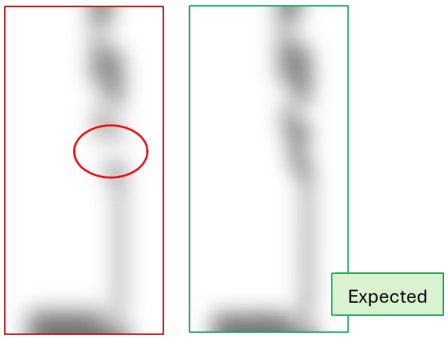

Figure 5.2: Separated 2D fluid domain caused by pairwise alignment of duct holes compared to the desired outcome

The final step in the preparation of the two-dimensional model consists of translating and rotating the solid bodies such that the selected section used to generate the 2D domain lies on the (z=0) plane, while the symmetry axis coincides with the (x)-axis. This specific orientation is required to perform the *badging* operation, through which STAR-CCM+ recognizes the geometry as a two-dimensional. The (x)-axis alignment, instead, is necessary to correctly enforce the axisymmetric assumption in the boundary conditions, allowing the solver to formulate the governing equations in terms of quantities per unit radian rather than per unit width. Once the parts have been properly badged, the corresponding planar section can be extracted and converted into the deseired 2D computational region on which the mesh generation process is subsequently carried out. A schematic overview of the adopted workflow and outcomes of each stage of the procedure is provided in Fig. 5.4.

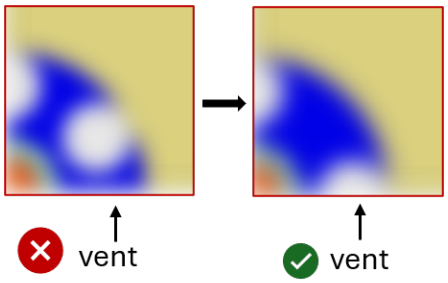

Figure 5.3: Change of the original geometry to create a continuous passage on the section of interest, preparatory to the 2D fluid domain extraction

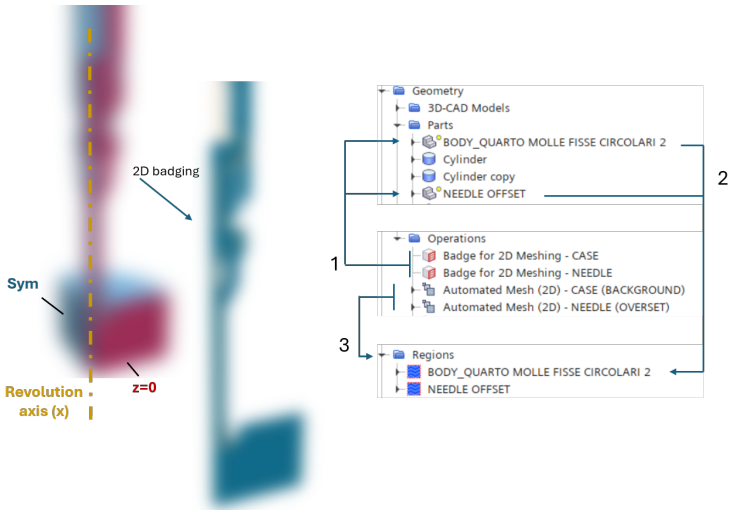

Figure 5.4: extraction of the 2D fluid domain: 1) the badging operation marks the parts with a yellow label to recognize the z=0 plane as a 2D domain; 2) the regions associated to the 2D section are created; 3) the 2D meshes associated to the related regions are created

5.2 Model setting

Once the geometric model and the associated computational regions have been prepared, the pre-processing phase must be completed with the definition of the numerical and physical set up adopted to the finalization of the overset-based DFBI formulation and fluid model.

5.2.1 Overset settings

Following the creation of the background and overset regions, the first step required to complete the overset setup consisted in assigning the *"Overset"* mesh boundary type to the outer surface of the needle-offset region, referred to as the *overset boundary*. This boundary defines the outer limit of the moving overset mesh and allows STAR-CCM+ to identify the region where information must be exchanged with the surrounding background grid through interpolation. The overset coupling was then established by creating an *"Overset Interface"* between the two regions. During the overset connectivity process, this interface enables the solver to classify cells according to their role within the interpolation scheme (active, donor, acceptor, or inactive cells) and to transfer the flow-field information between the overlapping meshes. Particular attention was devoted to the treatment

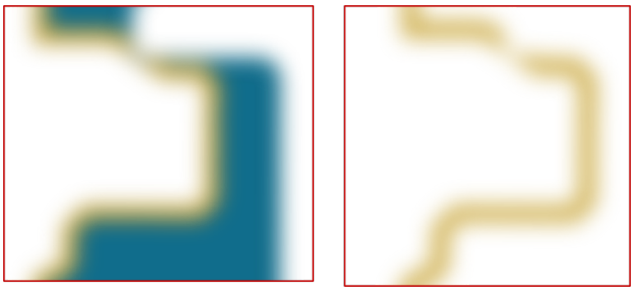

Figure 5.5: Failure of the standard overset coupling algorithm during gap closure: erroneous mesh classification results in the undesired removal of background cells (blue region) near the closing gap;

of the seal closure, where the moving seal surfaces come into contact with the stationary casing walls. To accurately handle this condition, the *"Zero Gap"* interface option was adopted. This formulation is specifically designed for overset applications involving closing gaps, automatically deactivating the cells trapped within the narrowing clearance when the distance between opposing walls becomes smaller than a prescribed number of cell layers. Simultaneously, a temporary *zero-gap wall boundary* is generated to prevent fluid leakage through the sealed region and to reproduce the physical closure of the gap. Finally, the *Alternate Hole Cutting* algorithm was activated within the overset-interface settings. Compared with the standard cutting procedure, this approach provides greater robustness when dealing with moving boundaries and gap-closure events, preventing the risk of numerical instabilities associated with the role change of the overset and background meshes, as shown in Fig. 5.5.

5.2.2 Physic setting

The physical models adopted to reproduce the injector operating conditions are summarized below:

- **Implicit unsteady:** only compatible choice with the overset-mesh methodology that accounts for the time-dependency of the flow field;
- **axisymmetric:** employed to apply the geometric symmetry of the model and solve the governing equations in terms of quantities per unit radian;
- **multi-component gas:** a mixture H_2 - air is considered to accurately capture the density

variations associated with flow expansions;

- **Real gas state equation**
- **segregated solver:** selected for its robustness and lower computational cost in transient simulations involving moving meshes;
- **RANS $k-\omega$ SST equation model**
- **All y+ wall treatment**

The axisymmetric formulation was completed by assigning the "*Axis*" boundary type to all boundaries lying on the symmetry axis of the model (the (x)-axis of the laboratory coordinate system). This setting ensures the correct treatment of the governing equations and the interpretation of flow quantities on a per-radian basis. Within the overset region, all boundaries were defined as no-slip walls, with the exception of the outer offset surface, which was assigned the *Overset Boundary* type to enable mesh coupling with the background region. The boundaries of the background region were instead configured following the same strategy adopted for the steady-state simulations. The only significant difference concerns the inlet boundary of the upstream reservoir. Although a *Stagnation Inlet* condition was again employed, the inlet pressure was prescribed through a *Table (Time)* profile reproducing the experimentally measured pressure trace. The flow field was initialized at rest, with the needle seal separating the domain into two regions characterized by the nominal inlet and outlet pressures upstream and downstream of the sealing surface, respectively. This initialization generates an initial pressure discontinuity across the closed valve equal to the design pressure ratio, providing a physically consistent starting condition for the transient simulation. Finally the time step has been defined such that to:

- **respect overset mesh requirements:** time step should be chosen so that the overset mesh does not move in the overlapping zone, within one time step, more than half the smallest cell size in this zone;
- **process the whole Δp at seal gap:** in order to let the segregated solver manage the high pressure drop at the beginning of the simulation, very small time steps were used to avoid numerical instabilities;

Following this two constraints, the time step has been tabled after some sensitivity tests in order to provide a suitable compromise between numerical stability and overset-mesh robustness, while maintaining an adequate temporal resolution of the flow evolution.

5.2.3 DFBI body and forces

The modeling of the actual needle motion is achieved through the creation of a *6-DOF DFBI Body*. Once associated with the needle overset region, this object treats the region as a rigid body with prescribed inertial properties, whose motion is computed as part of the solution from the balance of the external actions acting on it. To enable the computation of the needle motion through the DFBI framework, two main steps are required:

- **definition of DFBI motion**: a *DFBI Rotation and Translation* motion must be defined and assigned to the motion specifications of the overset region to rigidly move according to the displacement and rotation computed by the DFBI solver;
- **characterization of the needle dynamic:** the kinematic characteristics of the rigid body motion and the external loads acting on the body must be defined through the creation of a *continuum body*, which is subsequently associated with the needle overset region;

The first step consists of defining the motion properties of the overset region, which are configured such that the needle mesh follows the rigid-body motion computed by the DFBI solver for the body center of mass. This operation simply establishes the link between the body dynamics and the mesh motion, allowing the overset grid to translate consistently with the predicted needle displacement. The second step involves the definition of the actual computational body and its inertial properties, which govern the resulting motion. To this end, a *Continuum 2D Body* was associated with the needle wall boundaries, enabling the DFBI solver to account for the fluid-dynamic forces exerted on the valve surfaces in addition to the user-defined external loads. The kinematic behavior of the body was specified through the definition of its unconstrained degrees of freedom. Owing to the axisymmetric nature of the model, the *Axisymmetric Translating Motion* option was the only available choice, which restricts the body motion to the axial direction while remaining fully consistent with the physical displacement of the needle. The dynamic response of the body was then characterized by prescribing its mass and the forces acting upon it. In particular, the body

mass was defined as the equivalent mass per unit radian of the actual needle, in accordance with the axisymmetric formulation. The complete set of external and fluid-dynamic loads governing the needle motion during the simulation are applied to the body by creating appropriate *Force CM* objects (forces applied to the 6-DOF body center of mass) which are summarized below:

- **spring forces**: the springs contributions were modeled through the Hooke's law, based on the relative stiffness coefficients and instantaneous needle displacement, starting from their preloaded configuration;
- **seal reaction:** the seal force is similarly modeled through a linear elastic relation, which is active during compression and progressively vanishes once seal decompression is completed;
- **bellow contribution:** a displacement-independent force term is included to account for the bellow effect, modeled through an empirical relation based on the local pressure level;
- **Magnetic force:** this force represents the input provided by the actuation system and is prescribed as a function of needle lift through a tabulated set of curves; the force magnitude is obtained by interpolation of this curves as a function of the instantaneous needle position computed (see Fig. 5.6);
- **Fluid force:** resultant of the pressure and viscous shear stresses acting on the wall boundaries of the needle;
- **Max Lift Force:** artificial constraint force introduced to limit the needle stroke within the physically admissible range of the injector assembly, compensating for the absence of a more detailed mechanical interaction model;

All the aforementioned force contributions, with the exception of the fluid-dynamic term, are defined in magnitude through an *Expression Report*, which provides their intensity per unit radian as a function of the needle lift. The corresponding directions are specified through vector components, ensuring that each contribution is consistently projected along the needle axis with an appropriate sign. The evaluation of the fluid force requires particular attention. In general, the DFBI framework is capable of directly computing the resultant forces and moments acting on the DFBI body surfaces. However, when comparing this output with a standard *Force Report* defined on the same set of

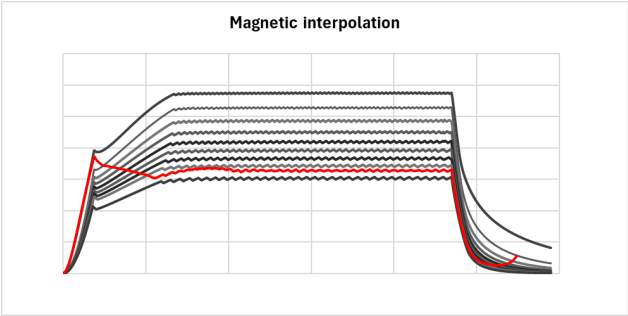

Figure 5.6: Interpolation in time of parametrized magnetic input: the magnetic force magnitude over time is parametrized as function of the needle displacement; basing on the displacement computed by the DFBI solver, the magnitude of the actuation system is interpolated through the curves;

needle surfaces, significant discrepancies were observed, particularly in the sign value, with the surface-based report providing results that are more consistent with the expected physical effect. A similar inconsistency was also found when comparing the DFBI fluid force obtained in the overset formulation with the corresponding DFBI force computed using the morphing-based approach, with which the surface force report showed full agreement. This mismatch is likely related to the way the overset methodology treats the needle surfaces during the simulation, especially the ones out of the background mesh. In contrast to the standard force report or the morphing strategy — where the effective fluid-wetted surfaces are obtained through subtraction operation performed upstream the mesh generation — the overset formulation preserves the original mesh geometry throughout the computation. As a consequence, the DFBI force evaluation in the overset model may effectively "see" a closed body representation rather than a holed surface configuration defined by the Boolean operation between parts, leading to a systematic overestimation and, in some cases, a sign inversion of the resulting force. The origin of this discrepancy can therefore be traced back to the different ordering of operations in the overset and morphing workflow. In the former the meshes are generated downstream of the regions creation. Thereby, the two grids are kept in background as inputs to update the pseudo subtract operation performed by the hole cutting process time-step per time-step. In the DFBI morphing model, instead, the region is created and updated in time downstream of Boolean subtract operation between the CFD part objects. This different processes return a different topology of the DFBI body surfaces which lead to the discrepancy of the fluid force reports. Indeed, the surface based report in the overset model computes the fluid forces over

the active walls resulting from the hole-cutting process, in a similar way the DFBI-fluid report in the computes the pressure contribution over the subtracted part mesh in the motphing motion strategy. For this reason, the surface-based *Force Report* was selected as the reference method for evaluating the fluid–structure interaction loads, as it provides results consistent with both the morphing formulation and the expected physical behavior.

5.2.4 Overset mesh

A critical factor in successfully applying the overset mesh methodology is to have comparable mesh resolution within the overlapping region between the background and overset grids. This overlapping zone must contain at least 4–5 cell layers in both background and overset meshes, between the solid walls and the overset boundary. The reasons for respecting this two simple but strict rules are many:

- ensuring grid densities of the same order of magnitude in the overlapping zone minimizes interpolation errors during the transfer of flow variables between the two meshes;
- the coarser grid of coupled mesh system effectively governs the interpolation accuracy, meaning that an excessively fine overset resolution cannot compensate for a poorly resolved background mesh and may even amplify numerical inconsistencies;
- the hole-cutting and connectivity algorithms require a minimum number of cell layers to correctly identify donor and acceptor cells throughout the relative motion of the overset region and ensure a stable data exchange;
- adequate overlap is necessary to successfully initialize the overset mesh interface between regions, allowing the background cells to be consistently deactivated and replaced by the overset region.

The mesh must fulfill all required features, otherwise the hole cutting process is likely to fail. Moreover, in moving overset configurations, such as the present needle motion case, since the overset interface is continuously updated at every time step it is possible that one of the requirements is violated at only one particular time. Therefore, designing the overset and background meshes

Mesh parameters	*Mesh 1*	*Mesh 2*	*Mesh 3*
Background			
Base size	0.2 mm	0.2 mm	0.4 mm
(min - max)	0.04mm - 0.1mm	0.04mm - 0.1mm	0.2mm - 0.3mm
Needle			
Base size	0.2 mm	0.2 mm	0.2 mm
(min - max)	0.04mm - 0.05mm	0.04mm - 0.1mm	0.04mm – 0.1 mm
Prism Layer			
Near Wall Thickness	5e-4mm	5e-3mm	5e-3mm
Total Thickness	0.02 mm	0.02 mm	0.2 mm
Number of layers	15	3	3
Custom Controls			
Overlapping area (backg.)	0.05 mm	0.05 mm	0.1 mm
Seal backgr.	0.04 mm	No controls	0.08 mm
Seal Needle	0.04 mm	No controls	0.05 mm
Poppet	0.08mm	No controls	No controls
TOT cell number	500k	196k	60k

Table 5.1: Mesh parameters

requires careful assessment of all possible positions during the simulation, which can be verified through preliminary mesh-preview runs using only the spatial and temporal discretization models. Basing on these guidelines three meshes with decreasing level of detail, respectively named "*Mesh 1*", "*Mesh 2*", "*Mesh 3*", were generated in order to take advantage of lower computational cost of the 2D framework, and subsequently to perform a mesh-sensitivity analysis in preparation for potential extension to a full 3D model, based on a less dense 2D baseline mesh. The corresponding mesh parameters are reported in Table 5.1. *Mesh 1*, featuring the highest resolution, was selected as the reference for the baseline results. All meshes were generated using a *polyhedral 2D mesher* combined with a *prism layer mesher* based on a wall-thickness formulation. To ensure consistent resolution within the overlap region, the background mesh was locally refined around the needle-

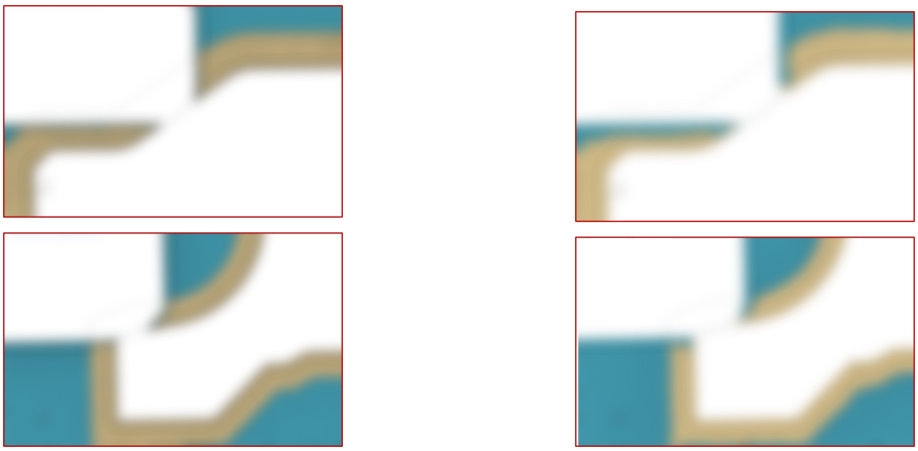

(a) (b)

Figure 5.7: Geometric detail level difference of zero-gap regions: (a) accurate representation of original surface geometry by Mesh 1 surface cut-off , (b) coarser representation of same surfaces in Mesh 2

offset area, while additional volumetric controls — similar to those employed in the steady-state model — were initially introduced in the seal and poppet regions. In an effort to reduce the overall computational cost in the other two mesh configurations, the boundary-layer discretization was minimized, as wall shear stresses were not expected to be the dominant contribution to the needle force balance. Further simplifications, in Mesh 2, were introduced by removing most of the volumetric refinements, relying instead on the base mesh resolution only. However, this led to a reduction in geometric fidelity in regions where intersecting walls are handled through the zero-gap formulation, due to the increased cell size involved in the gap closure generation (see Fig. 5.7). As a consequence, the lower extension of active surfaces reduced the effective contribution of pressure forces from certain needle components, affecting the predicted opening and closing dynamics of the needle. To mitigate this effect, *Mesh 3* reintroduced localized volumetric refinement only in the seal region, taking advantage of a coarser background mesh while restoring the low geometric detail level. This strategy allowed the total cell count to be limited to approximately 60k elements, compared to the initial 500k of the most refined configuration.

5.3 Result analysis

The overset simulations immediately highlighted one of the main challenges associated with this methodology, namely the definition of a suitable time-step size. As discussed in Section 5.2.2, the time step must simultaneously satisfy the constraints imposed by the overset connectivity algorithm and ensure the numerical stability of the flow solution. In the present application, these requirements proved particularly restrictive during the opening of the seal gap, where extremely small time steps were necessary to avoid both mesh-related and numerical instabilities. This behavior revealed a critical aspect of overset simulations involving *zero-gap interfaces*. In particular, the most delicate phase occurs when cells that were previously inactive become active as the gap starts to open. Under these conditions, the newly activated cells are suddenly exposed to the large pressure difference, which can compromise the stability of the solution if the temporal discretization is insufficient. Conversely, no comparable issues were observed during the closing stroke, as illustrated in Fig. 5.8. During the injector closure, the flow field evolves from an already established solution and the pressure distribution is significantly more uniform throughout the domain. The cells located within the closing clearance are simply deactivated by the zero-gap algorithm, while the remaining active cells continue to evolve according to the updated boundary conditions without introducing severe numerical disturbances. The adoption of very small time steps during the initial opening phase therefore proved essential not only for the stability of the overset connectivity but also for the reliability of the predicted flow quantities. In fact, an inadequate temporal resolution would lead to spurious oscillations of the field variables throughout the simulation, which would directly affect the accuracy of the quantities of interest, such as the mass flow rate and the fluid-dynamic force acting on the needle. Considering the mass-flow-rate predictions and their comparison with both

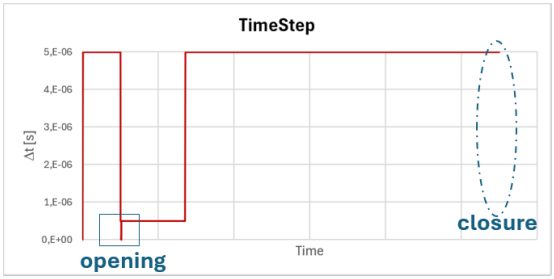

Figure 5.8: time-step definition for *Mesh1* overset model: no time-step criticalities at closure

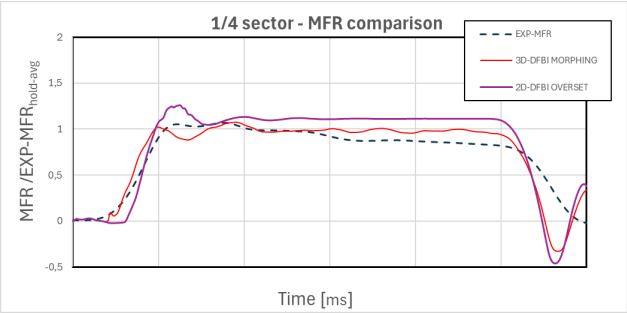

Figure 5.9: Mass Flow Rate DFBI models comparison respect to average experimental value at max operating conditions

the experimental measurements and the morphing counterpart of the DFBI model, Fig. 5.9 shows a generally good agreement throughout the entire injection cycle. From a dynamic perspective, the overset model reproduces the measured mass-flow-rate gradients with remarkable accuracy during the different phases of the event, confirming its ability to capture the dominant physical mechanisms governing the injector operation. The only noticeable discrepancy is observed during the closing stage, where the flow response predicted by the overset model exhibits a slightly lower inertia than the experimental trace. Furthermore, the strong agreement with the morphing-based simulation highlights the consistency of the DFBI formulation in forecasting very similar mass-flow-rate evolutions despite the fundamentally different motion strategy adopted. This result is particularly significant considering that the overset model relies on a two-dimensional axisymmetric approximation, thus requiring a substantially lower computational effort than the corresponding three-dimensional simulation. To quantify the level of accuracy independently of the transient dynamic, the numerical results were sampled at selected operating conditions, similarly to the SS approach, and compared with the corresponding experimental mass-flow-rate values, as shown in Fig. 5.10. This procedure enables a point-by-point comparison between numerical and experimental data at equivalent operating conditions.In this way, the influence of the simulation history is filtered out, allowing the accuracy of the predicted flow conditions to be evaluated directly. The sampling analysis highlights even more clearly the systematic tendency of the overset model to overpredict the mass flow rate. Nevertheless, apart from a limited number of isolated peaks, the relative-error distribution reported in Fig. 5.11a shows that the average error remains below 20%, corresponding to only a few grams per second in absolute terms. This overestimation is likely associated with the

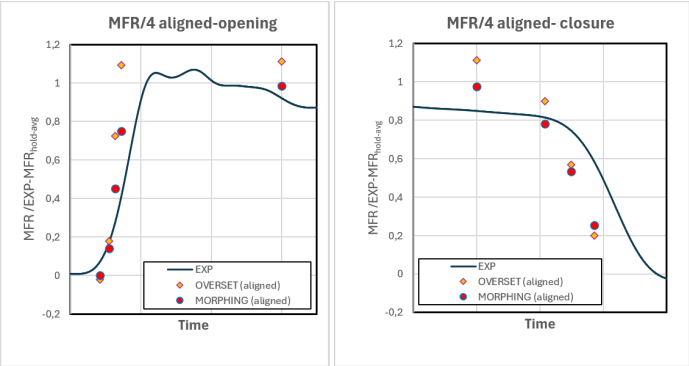

Figure 5.10: DFBI models sampling and predictions according to reference experimental MFR positions

geometric simplifications introduced during the generation of the two-dimensional axisymmetric model. In particular, the modifications required to obtain a continuous representative section may result in a slightly larger effective flow area than that of the original three-dimensional geometry. This interpretation is further supported by the comparison with the experimental data shown in Fig. 5.11b. Although the morphing model generally provides a more accurate prediction, both numerical approaches exhibit a similar error distribution and trend, suggesting that the dominant source of deviation is related to the geometric approximation rather than to the overset methodology itself. Respect to the measured dataset, the largest discrepancies are observed near the opening and closing phases of the injector, where transient effects are most pronounced and the solution becomes particularly sensitive to the local flow conditions. In these regions, the influence of the initial conditions, the rapid evolution of the pressure field, and the activation or deactivation of

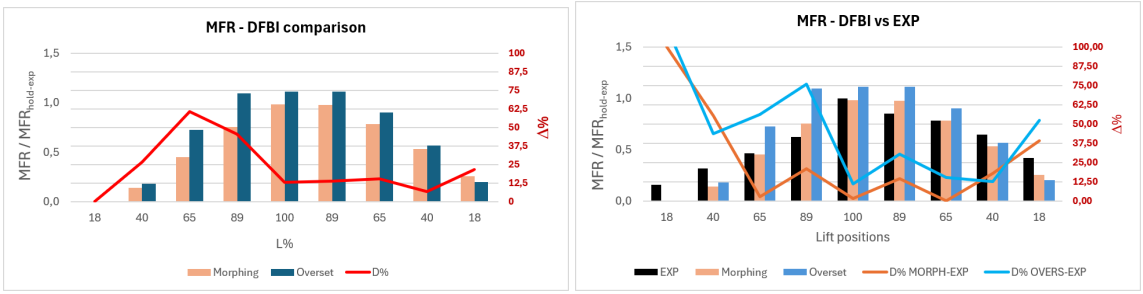

(a) (b)

Figure 5.11: Normalized MFR comparison with distribution of the relative error along the relevant lift positions

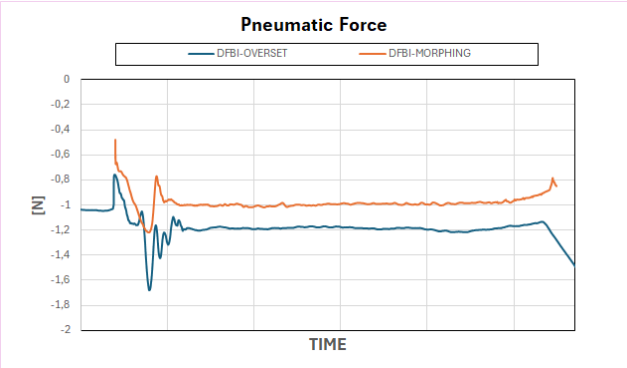

Figure 5.12: DFBI comparison of normalized Fluid force report respect to the average holding value for the different motion strategy considered

cells associated with the zero-gap treatment in the overset contribute to the increased uncertainty of the numerical predictions. The tendency of the two-dimensional overset model to overpredict the flow quantities is also reflected in the computed fluid-dynamic forces. As shown in Fig. 5.12, the overall force evolution closely follows the trend predicted by the morphing model, while additionally capturing the pressure-field dynamics associated with seal compression and decompression. These effects, which could not be fully reproduced by the morphing-based DFBI approach, result in a force trace that exhibits greater continuity with the interrupted opening and closing transients of the comparative model. This improved physical representation, however, comes at the expense of a higher level of oscillations and a reduced local accuracy during the seal-opening phase, where the sudden expansion of the flow generates strong transient effects and numerical instabilities. Overall, the overset model predicts fluid forces approximately 30% higher than those obtained from the three-dimensional morphing simulation. This discrepancy is consistent with the slightly higher pressure levels observed in this model and should be assessed more rigorously through a dedicated three-dimensional overset model. Nevertheless, considering the exploratory nature of the present investigation and the simplifying assumptions introduced by the two-dimensional axisymmetric formulation, this level of deviation can still be regarded as acceptable for preliminary design purposes. Despite the overestimation of the fluid force, the needle trajectory predicted by the DFBI solver shows excellent agreement with the morphing solution throughout most of the injection cycle. The main differences are confined to the initial opening phase of the valve, where the two approaches are characterized by fundamentally different initial conditions. In the

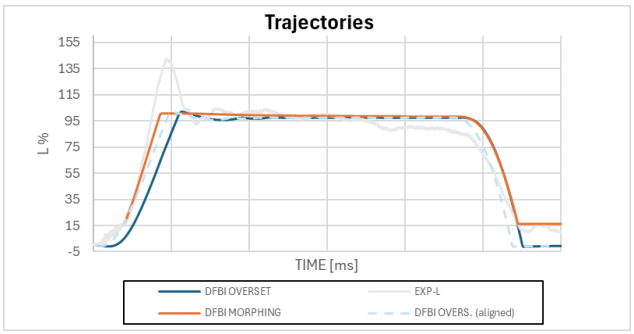

Figure 5.13: Comparison of DFBI models needle displacements with respect experimental measured one

morphing-based DFBI model, the simulation starts from an already open configuration because contact between moving and stationary surfaces cannot be represented. Consequently, the initial velocity and acceleration of the needle must be reconstructed from the experimental measurements to reproduce the actual injector dynamics. In contrast, the overset formulation starts from the physically realistic closed-seal configuration and computes the needle motion directly from the balance of the applied forces. As a result, the differences observed during the opening stroke can be primarily attributed to the modeling of the seal decompression process, since the seal reaction constitutes the only additional force contribution with respect to the morphing formulation. In particular, the lower decompression velocity predicted by the overset simulation suggests that the equivalent seal stiffness may be underestimated. Nevertheless, when compared with the experimental needle-lift trace, the displacement predicted by the DFBI solver remains sufficiently accurate, especially considering that the motion is obtained exclusively from the prescribed external loads and the computed fluid forces, without any artificial imposition or alignment to the measured trajectory, apart from the max lift force imposed to limit the stroke of the needle to account for the actual geometric constraints of exciting pin stroke. This capability makes the overset-based DFBI approach the most physically representative methodology investigated for supporting the virtual design and development of the injector, in absence of experimental indications.

5.3.1 Mesh sensitivity

The mesh-sensitivity analysis, performed as a preliminary step toward the development of a future three-dimensional overset model, immediately highlighted the trade-off between computational

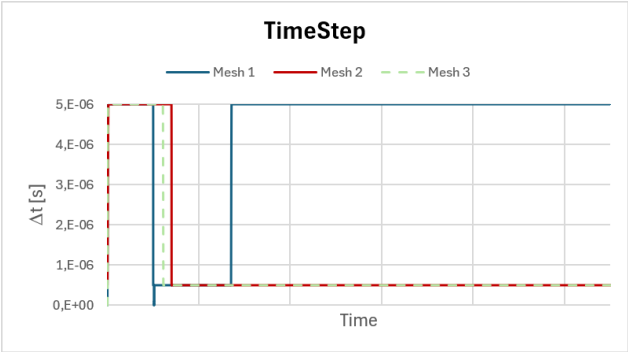

Figure 5.14: Simplification of time-step strategy enabled by lower mesh resolution and solver options

efficiency and solution accuracy. While reducing the number of cells significantly decreases both computational cost and model complexity, it also leads to a loss of grid resolution in critical flow regions, with consequent impacts on numerical robustness and prediction accuracy. In particular, the simulations performed with *Mesh 2* and *Mesh 3* required specific numerical treatments to overcome the instabilities arising during the opening of the seal gap, where the sudden activation of cells subjected to a large pressure difference often caused solution divergence. For *Mesh 2*, the issue was successfully addressed by enabling the *Overset Conservation* option, which enforces conservation of mass across the overset interface, mitigating the strong oscillations that would be obtained otherwise. The same strategy, however, proved ineffective for *Mesh 3*, whose coarser discretization and different base-size definition resulted in a more challenging overset coupling. In this case, stable solutions were obtained by adopting the *Linear Quasi-2D* interpolation scheme at the overset interface. This interpolation method is particularly suited to grids characterized by a limited number of cells across the thickness direction (usually one layer), such as those generated by the coarse zero-gap configuration. The adoption of these numerical workarounds not only improved the robustness of the simulations but also substantially simplified the time-step strategy adopted by the reference mesh (see Fig. 5.14). As a consequence, the overall computational effort was significantly reduced: despite a reduction of approximately 90% in the total cell count, the coarser meshes were able to provide accurate average solutions while decreasing the simulation time by nearly a factor of two (from 13h to about 6 hours). As expected, the reduction in grid resolution resulted in a decrease in the accuracy and smoothness of the predicted quantities. The mass-flow-rate and fluid-force histories reported in Figs. 5.15a and 5.15b show a progressively

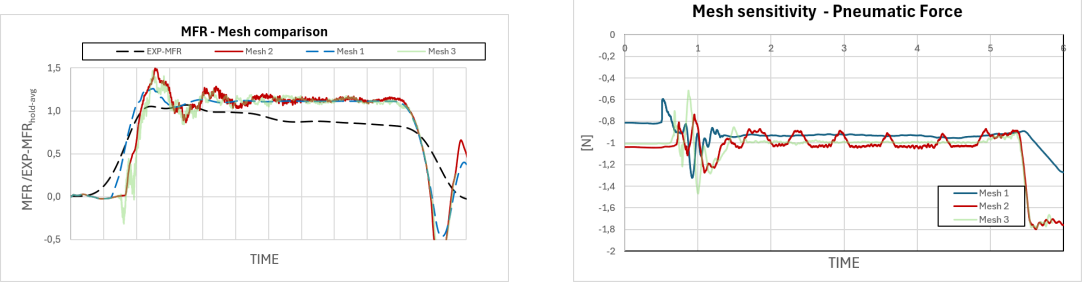

(a) (b)

Figure 5.15: Mesh sensitivity: (a) MFR normalized respect to EXP reference value, (b) Fluid Force normalized respect to Mesh 1 holding average value

higher level of oscillations as the mesh is coarsened. This behavior is particularly evident at large needle lifts, where the overset interface plays a more significant role and the mismatch between the background and overset grids becomes more sensitive. Under these conditions, interpolation errors across the overlapping region are superimposed on the discretization errors associated with the lower mesh resolution, leading noisier solutions. The poorer geometric detail, instead, affected the definition of the fluid force along the seal compression parts of the cycles (initial and final), leading to the overestimation of the pressure actions produced by the smaller surface extension of the active walls returned by the zero-gap model. As a result, the needle opening is delayed due to the larger force required respect to the finer reference case (Mesh 1), an effect that is further enhanced at the beginning of the following cycles due to new pressure distribution achieved by flow in between two injection cycles.

6. Final considerations

The analysis of the two approaches carried out so far allows a comprehensive comparison of the different CFD methodologies investigated for the simulation of the high-pressure hydrogen injector. From the mass-flow-rate perspective, all the methodologies proved capable of predicting the injector performance with a satisfactory level of accuracy, particularly during the holding phase of the lift law, where the valve operates under quasi-steady conditions and reaches its maximum flow capacity. Under these circumstances, the steady-state approach emerged as the most effective solution, providing predictions in close agreement with the experimental measurements while requiring only a fraction of the computational resources demanded by the transient methodologies. Furthermore, when the numerical results were compared at equivalent operating conditions, independently of the simulation history, the steady-state simulations showed a level of accuracy comparable to that achieved by the DFBI approach, as can be observed in the spiderchart in Fig. 6.1. A similar conclusion can be drawn regarding the fluid-dynamic forces acting on the needle. The steady-state approach proved capable of accurately reproducing the global effects of the pressure field and the average fluid loads predicted by the transient methodologies whenever the needle motion remained aligned with the flow direction or the accelerations were sufficiently small. In these conditions, the agreement between stationary and transient simulations remained remarkably good, confirming the ability of the steady-state methodology to provide meaningful estimates of the fluid-structure interaction loads required during the preliminary design stages. Conversely, larger discrepancies

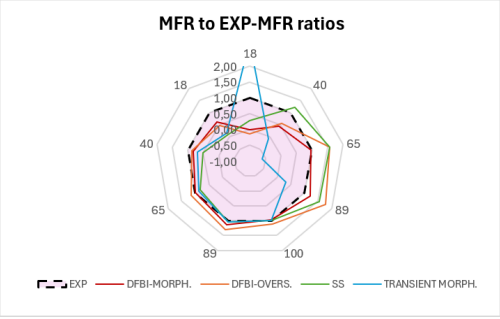

Figure 6.1: CFD methodologies comparison: values of MFR at relevant lift positions normalized to the respective experimental value

were observed during the final portion of the closing stroke, where the needle retracts against an already established flow field and the dynamics become dominated by strongly transient phenomena. Although the steady-state model correctly captured the overall trend of the force evolution, the results are strongly affected by the mid-chamber pressurization. Indeed, the transient simulations provided a more reliable representation of the local pressure redistribution occurring during chamber isolation and seal closure, leading to a more closing attitude of the flow shared by all the unsteady models. Despite their superior physical fidelity, transient methodologies inevitably require a significantly larger computational effort and a considerably more demanding setup procedure. In this respect, the DFBI–overset formulation emerged as the most promising unsteady approach investigated in this work. Even in its simplified two-dimensional implementation, it proved capable of providing fast and more simplified mesh motion setup and optimization other than handling contact-like conditions between moving and stationary surfaces, reproducing the expected injector dynamics with good consistency relative to the reference transient model but without relying on experimentally prescribed needle trajectories. This characteristic makes the overset-based DFBI framework particularly attractive for the design process whenever a deeper understanding of the governing physics is required or experimental information are unavailable, provided that a high geometric detail of the wall surfaces is guaranteed.

6.1 Conclusions

The comparative analysis carried out throughout this work therefore highlighted the strengths, limitations, and fields of applicability of the different numerical methodologies investigated for the simulation of a high-pressure hydrogen injector. Despite the strong simplifying assumptions introduced, the steady-state approach demonstrated a remarkable capability to reproduce the experimental mass-flow-rate measurements and the average flow conditions predicted by the transient models. In particular, the agreement observed during the quasi-stationary phases of the injection cycle and the relatively small discrepancies in the prediction of the fluid-dynamic forces confirm the suitability of steady-state simulations as efficient design-support tools during the preliminary stages of injector development. Their low computational cost, ease of setup, and robustness make them particularly attractive for rapid design iterations and for generating performance maps to be coupled

with lower-order system models. On the other hand, the transient methodologies proved essential for capturing the inherently time-dependent phenomena that characterize the opening and closing phases of the injector. The morphing approach provided valuable insight into the evolution of the flow field when the needle motion is prescribed, whereas the DFBI–overset formulation enabled the injector dynamics to be reconstructed directly from the balance of fluid and external forces. Although computationally more demanding and numerically more complex, these approaches offer a deeper understanding of fluid–structure interactions, pressure-wave propagation, flow-history effects, and transient compressible-flow phenomena that cannot be reproduced by stationary simulations.

Overall, the results suggest that steady-state and transient approaches should not be regarded as competing methodologies, but rather as complementary tools within a unified design framework. The steady-state approach offers the best compromise between accuracy, robustness, computational efficiency, and ease of implementation, making it the preferred solution for routine design activities and preliminary design assessments, while transient models provide the level of physical fidelity required for detailed validation, optimization, and investigation of complex dynamic phenomena during th final stages of the design process.

Bibliography

[1] *The European Green Deal*. URL: https://commission.europa.eu/strategy-and-policy/priorities-2019-2024/european-green-deal_en.

[2] *Greenhouse gas emissions from transport in Europe*. 2025. URL: https://www.eea.europa.eu/en/analysis/indicators/greenhouse-gas-emissions-from-transport?activeAccordion=546a7c35-9188-4d23-94ee-005d97c26f2b.

[3] Xue Dong et al. "CO2 Emission of Electric and Gasoline Vehicles under Various Road Conditions for China, Japan, Europe and World Average—Prediction through Year 2040". In: *Applied Sciences* 9.11 (2019). ISSN: 2076-3417. DOI: 10.3390/app9112295. URL: https://www.mdpi.com/2076-3417/9/11/2295.

[4] Angelo Onorati et al. "The role of hydrogen for future internal combustion engines". In: *International Journal of Engine Research* 23 (Apr. 2022), pp. 529–540. DOI: 10.1177/14680874221081947.

[5] Ho Lung Yip et al. "A Review of Hydrogen Direct Injection for Internal Combustion Engines: Towards Carbon-Free Combustion". In: *Applied Sciences* 9.22 (2019). ISSN: 2076-3417. DOI: 10.3390/app9224842. URL: https://www.mdpi.com/2076-3417/9/22/4842.

[6] A. Onorati and G. Montenegro. *1D and Multi-D Modeling Techniques for IC Engine Simulation*. SAE International, 2020. ISBN: 9780768099522. URL: https://books.google.it/books?id=63h0EAAAQBAJ.

[7] Sebastiano Breda et al. "Computational study of injector cap design for optimized mixing and combustion in a high-performance DI hydrogen engine". In: *International Journal of Hydrogen Energy* 138 (2025), pp. 129–150. ISSN: 0360-3199. DOI: https://doi.org/10.1016/j.ijhydene.2025.05.085. URL: https://www.sciencedirect.com/science/article/pii/S0360319925023341.

[8] Nhlanhla Khanyi, Freddie Liswaniso Inambao, and Riaan Stopforth. "A Comprehensive Review of the GT-POWER for Modelling Diesel Engines". In: *Energies* 18.8 (2025). ISSN:

1996-1073. DOI: 10.3390/en18081880. URL:
https://www.mdpi.com/1996-1073/18/8/1880.

[9] M. Darwish F. Moukalled L. Mangani. *The Finite Volume Method in Computational Fluid Dynamics - An Advanced Introduction with OpenFOAM® and Matlab®*. Springer, 2015.

[10] Marcin Sosnowski. "The influence of computational domain discretization on CFD results concerning aerodynamics of a vehicle". In: *Journal of Applied Mathematics and Computational Mechanics* 17 (Mar. 2018), pp. 79–88. DOI: 10.17512/jamcm.2018.1.08.

[11] Marcin Sosnowski et al. "Polyhedral meshing in numerical analysis of conjugate heat transfer". In: *International Conference on Experimental Fluid Mechanics (EFM)* 180 (Jan. 2017), pp. 589–594. DOI: 10.1051/epjconf/201817002096.

[12] *Simcenter STAR-CCM+ 2410 User Guide*. URL:
https://docs.sw.siemens.com/en-US/doc/226870983/PL20240730373082998.starccmp_userguide_html?audience=external.

[13] Francesco Falcinelli. "Analisi CFD-3D del comportamento termico di un iniettore idrogeno di nuova concezione per motori heavy duty". MA thesis. Università degli Studi di Modena e Reggio Emilia, 2024.

[14] Joseph Majdalani Frank M. White. *Viscous Fluid Flow*. McGraw Hill.